Smart Quality Assurance System for Additive Manufacturing using Data-driven based Parameter-Signature-Quality Framework

Andrew Chung Chee Law

Dissertation submitted to the faculty of the Virginia Polytechnic Institute and State University in partial fulfillment of the requirements for the degree of

Doctor of Philosophy
In
Industrial and Systems Engineering

Zhenyu (James) Kong, Chair
Blake Johnson
Xiaowei Yue
Haibo Zeng

06/24/2022
Blacksburg, VA

Keywords: Additive manufacturing, bioprinting, scaffold porosity estimation, residual stress prediction, smart quality assurance, deep learning, artificial neural network, forward modeling, active learning, predictive uncertainty, inverse design

Smart Quality Assurance System in Additive Manufacturing using Data-driven based Parameter-Signature-Quality Framework

Andrew Chung Chee Law

ABSTRACT

Additive manufacturing (AM) technology is a key emerging field transforming how customized products with complex shapes are manufactured. AM is the process of layering materials to produce objects from three-dimensional (3D) models. AM technology can be used to print objects with complicated geometries and a broad range of material properties. However, the issue of ensuring the quality of printed products during the process remains an obstacle to industry-level adoption. Furthermore, the characteristics of AM processes typically involve complex process dynamics and interactions between machine parameters and desired qualities. The issues associated with quality assurance in AM processes underscore the need for research into smart quality assurance systems.

To study the complex physics behind process interaction challenges in AM processes, this dissertation proposes the development of a data-driven smart quality assurance framework that incorporates in-process sensing and machine-learning-based modeling by correlating the relationships among parameters, signatures, and quality. High-fidelity AM simulation data and the increasing use of sensors in AM processes help simulate and monitor the occurrence of defects during a process and open doors for data-driven approaches such as machine learning to make inferences about quality and predict possible failure consequences.

To address the research gaps associated with quality assurance for AM processes, this dissertation proposes several data-driven approaches based on the design of experiments (DoE), forward prediction modeling, and an inverse design methodology. The proposed approaches were

validated for AM processes such as fused filament fabrication (FFF) using polymer and hydrogel materials and laser powder bed fusion (LPBF) using common metal materials. The following three novel smart quality assurance systems based on a parameter–signature–quality (PSQ) framework are proposed:

1. A customized in-process sensing platform with a DOE-based process optimization approach was proposed to learn and optimize the relationships among process parameters, process signatures, and parts quality during bioprinting processes. This approach was applied to layer porosity quantification and quality assurance for polymer and hydrogel scaffold printing using an FFF process.
2. A data-driven surrogate model that can be informed using high-fidelity physical-based modeling was proposed to develop a parameter–signature–quality framework for the forward prediction problem of estimating the quality of metal additive-printed parts. The framework was applied to residual stress prediction for metal parts based on process parameters and thermal history with reheating effects simulated for the LPBF process.
3. Deep-ensemble-based neural networks with active learning for predicting and recommending a set of optimal process parameter values were developed to optimize optimal process parameter values for achieving the inverse design of desired mechanical responses of final built parts in metal AM processes with fewer training samples. The methodology was applied to metal AM process simulation in which the optimal process parameter values of multiple desired mechanical responses are recommended based on a smaller number of simulation samples.

Smart Quality Assurance System in Additive Manufacturing using Data-driven based Parameter-Signature-Quality Framework

Andrew Chung Chee Law

GENERAL AUDIENCE ABSTRACT

Additive manufacturing (AM) is the process of layering materials to produce objects from three-dimensional (3D) models. AM technology can be used to print objects with complicated geometries and a broad range of material properties. However, the issue of ensuring the quality of printed products during the process remains a challenge to industry-level adoption. Furthermore, the characteristics of AM processes typically involve complex process dynamics and interactions between machine parameters and the desired quality. The issues associated with quality assurance in AM processes underscore the need for research into smart quality assurance systems.

To study the complex physics behind process interaction challenges in AM processes, this dissertation proposes a data-driven smart quality assurance framework that incorporates in-process sensing and machine-learning-based modeling by correlating the relationships among process parameters, sensor signatures, and parts quality. Several data-driven approaches based on the design of experiments (DoE), forward prediction modeling, and an inverse design methodology are proposed to address the research gaps associated with implementing a smart quality assurance system for AM processes. The proposed parameter–signature–quality (PSQ) framework was validated using bioprinting and metal AM processes for printing with polymer, hydrogel, and metal materials.

DEDICATION

To all my family members, especially my spouse, for their unconditional love and support along the journey.

ACKNOWLEDGMENTS

I am grateful for having Dr. Zhenyu (James) Kong as my academic advisor and life mentor, who has dedicated and inspired me through this challenging yet rewarding journey to pursue my Ph.D. program at Virginia Tech. Along the journey, Dr. Kong is always supportive and resourceful in guiding me in any situation. In addition, I would like to extend my gratitude to my Ph.D. committee members: Dr. Blake Johnson, Dr. Xiaowei Yue and Dr. Haibo Zeng, for their continuous support and valuable suggestions on my research topics.

Furthermore, I am thankful to receive help and encouragement from awesome individuals I have met throughout my graduate study at Virginia Tech. I would like to thank my fellow lab members: Dr. Jia Liu, Dr. Chenang Liu, Dr. Bo Shen, Mr. Jihoon Chung, Mr. Rongxuan Wang, Ms. Maede Maftouni, and Mr. Benjamin Standfield.

Last but not least, I deeply appreciate the constant help from the faculty and staff of the Grado Department of Industrial and Systems Engineering at Virginia Tech. It is my pleasure to pursue my study and Ph.D. program with everyone I met in the department.

Table of Contents

List of Figures

List of Tables

1. Introduction

1.1 Background and motivation

AM technology is a key emerging field transforming how products are manufactured. In AM, materials are layered to produce objects from 3D models. AM technology can be used to print objects with complicated geometries and a broad range of material properties. However, the issue of ensuring the quality of printed products remains an obstacle to industry-level adoption. Furthermore, the characteristics of AM processes typically involve complex process dynamics and interactions between machine parameters and desired qualities. The issues associated with quality assurance in AM processes underscore the need for research into smart quality assurance systems.

A smart quality assurance system framework that can incorporate in-process sensing technology and utilize machine-learning-based modeling by correlating the relationships among process parameters, sensor signatures, and parts quality is proposed to address the complex physics behind process interaction challenges in AM processes. High-fidelity AM simulation data and the increasing use of sensors in AM processes help simulate and monitor the occurrence of defects during a process and open doors for data-driven approaches such as machine learning to make inferences about quality and predict possible failure consequences. Although simulation and experimental studies can provide high-quality data on AM processes, the high computational costs and time involved remain concerns at the industry level in implementing quality monitoring systems for AM processes. Hence, there is a pressing need for machine-learning-based forward modeling and inverse design as a high-fidelity and low-computational-cost surrogate modeling approach that relates desired quality characteristics to optimal input process parameter values.

1.2 Research objectives

This dissertation proposed a smart quality assurance system using a data-based parameter–signature–quality (PSQ) framework to address the research gaps associated with quality assurance for AM processes. This system is integrated with the design of experiments (DoE), forward prediction modeling, and inverse design across AM processes, namely, bioprinting and metal AM. The research had the following three specific objectives:

1. **Learning the relationship between process parameters, process signatures, and parts quality during bioprinting processes:** The question addressed was how to map process parameters corresponding to the quality characteristics of printed parts in an in-process quality monitor and control system?
2. **Developing a PSQ framework for forward prediction of the quality of metal additive-printed parts:** The question addressed was how to integrate simulation insights and surrogate modeling of the signature–quality relationship in the forward prediction of parts quality?
3. **Recommending optimal process parameter values to achieve the inverse design of desired mechanical responses of final built parts in metal AM processes with fewer samples:** The question addressed was how to optimize optimal process parameter values that will achieve the desired quality for the inverse design of a metal AM process with fewer training samples?

The contributions of this dissertation work can be summarized by the achievement of these three research objectives, as summarized by the following three points:

1. First, the work established a novel PSQ framework for correlating the relationships among process parameters, sensor signatures, and parts qualities for bioprinting processes using a customized in-process sensing platform and DoE approach.
2. Second, the work offered a deep-learning-based surrogate modeling solution for utilizing machine parameters and process signatures corresponding to mechanical responses for rapid residual stress estimation inference.
3. Third, the work explored the promising neural network architecture of deep-ensemble-based neural networks that employ predictive uncertainty and active learning to optimize optimal process parameter values of the inverse design of desired mechanical response requirements with fewer samples.

The potential extension of the proposed application frameworks to any AM process is demonstrated. The proposed data-driven PSQ framework can be applied to other areas of the manufacturing processes domain.

1.3 Dissertation organization

The remainder of this dissertation is organized as follows. The proposed research framework, related literature, and research gap analysis are presented in Chapter 2. In Chapter 3, a customized in-process DoE-based sensing platform is presented to demonstrate process parameter optimization for layer porosity quantification of polymer and hydrogel scaffold printing. In Chapter 4, a deep-learning-based surrogate modeling approach to utilizing the underlying process physics of AM simulation data is presented for the forward prediction of a metal AM process. Deep-ensemble-based neural networks that employ predictive uncertainty and active

learning to optimize the optimal process parameter values for the inverse design of desired mechanical responses are proposed in Chapter 5. In Chapter 6, the contributions of the research work and promising future research directions are summarized.

2. Research overview and literature review

2.1 Research overview

As described in Chapter 1, the goal of this dissertation research was to develop a smart quality assurance system framework that can correlate the relationship between process parameters, process signatures, and product quality for AM applications. As illustrated in Figure 2-1, the proposed research methodologies focus on establishing a data-driven parameter–signature–quality (PSQ) framework that integrates in-process sensing, statistical analysis methods, physics-based simulation data, advanced machine learning algorithms, and active learning-based inverse design. In this research framework, a customized in-process sensing platform is established to provide experimental in-process data. Finite element modeling (FEM) software is utilized to supply high-quality simulation AM data as process signatures for training and testing samples for deep learning approaches.

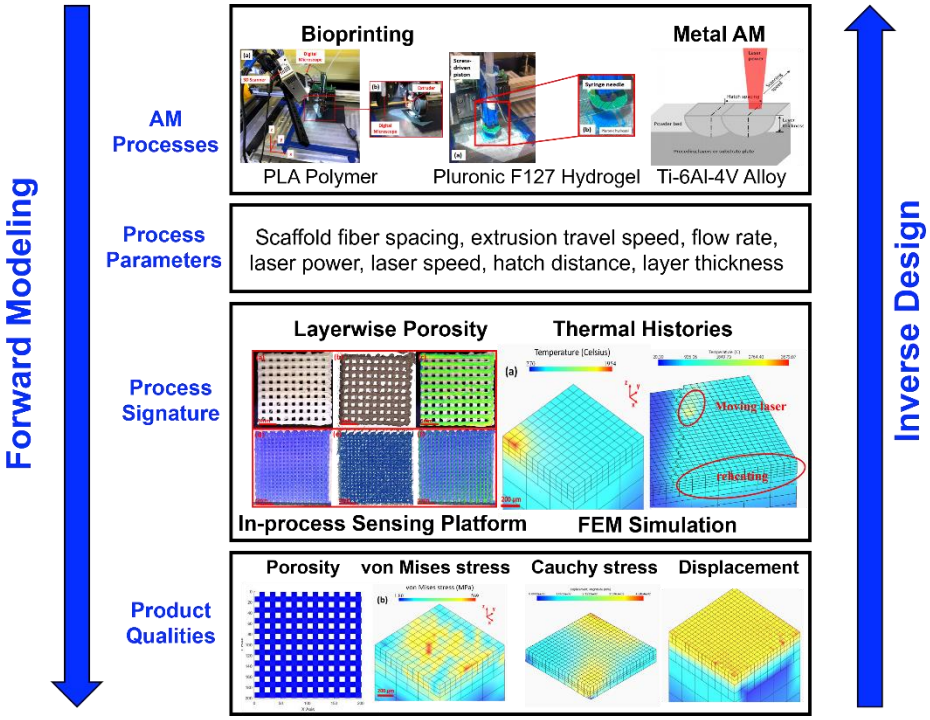

Figure 2-1: Overview of the proposed research PSQ framework.

Following this PSQ framework, the research goals were achieved by conducting three specific tasks, illustrated in Figure 2-2.

- Task 1: This task was to learn the relationship between process parameters and corresponding part quality using an in-process sensing platform integrated with statistical design-of-experiment techniques to implement proper process mapping and optimization for bioprinting (Chapter 3).
- Task 2: This task was to develop a deep-learning-based surrogate modeling approach using high-fidelity physics-based simulation AM data to take advantage of the reheating effects of thermal histories and process parameters for residual stress prediction for metal AM-printed parts (Chapter 4).
- Task 3: This task was to establish a sequential learning-based inverse design problem for optimizing optimal process parameters, given desired mechanical responses, using two deep-ensemble-based neural networks that employ predictive uncertainty and active learning (Chapter 5).

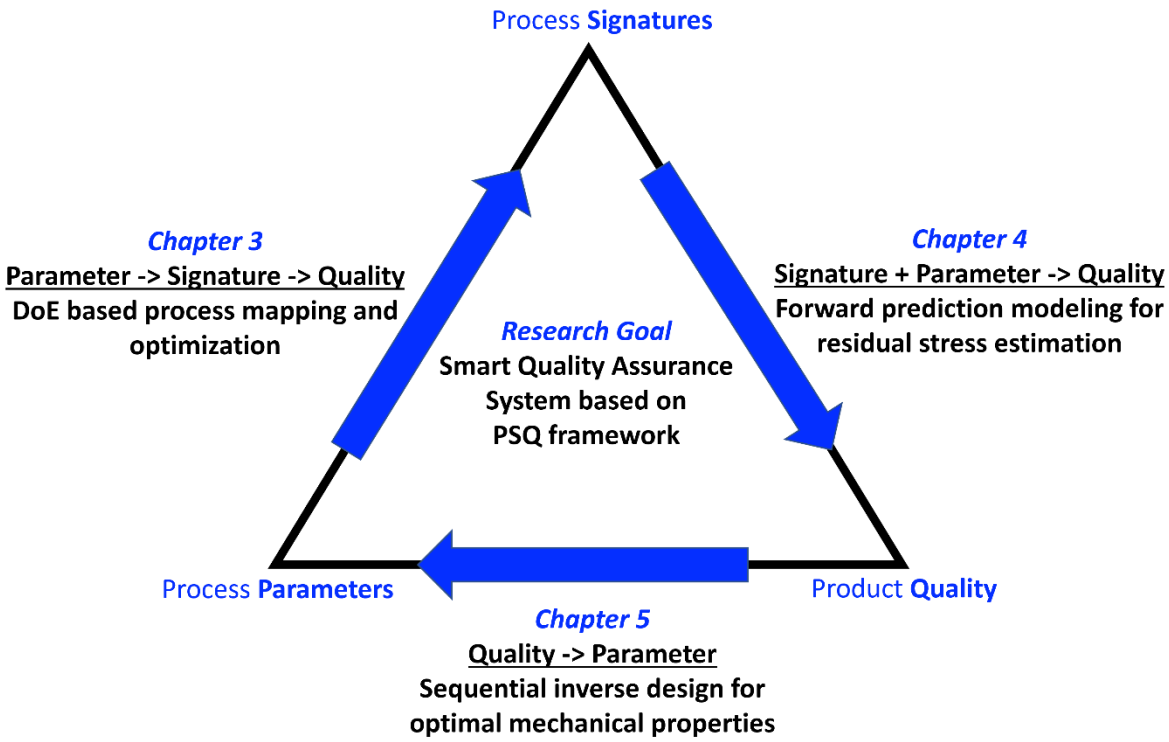

Figure 2-2: Overall structure of the proposed research PSQ framework.

2.2 Literature review

This research was motivated by the need for a smart quality assurance system for AM processes using a data-driven PSQ framework. Section 2.2.1 summarizes related studies on quality assurance of AM processes and the PSQ concept. Related studies on process parameter applications in bioprinting are reviewed in Section 2.2.2. The need for surrogate modeling in AM processes is described in Section 2.2.3. The literature on the forward prediction modeling of AM processes is summarized in Section 2.2.4. The application of inverse design to AM processes is reviewed in Section 2.2.5. The research gaps addressed by the current work are identified in Section 2.3.

2.2.1 Quality assurance of AM process

One of the challenges facing AM is quality assurance [1]. Many researchers have identified quality assurance and control as the greatest challenge to the industry-wide adoption of AM

technologies [1]. One active research initiative to improve the quality assurance of AM is to develop in situ process monitoring and control systems [2] that can correlate process parameters, process signatures, and product qualities. Mani *et al.* [3, 4] introduced the concept of process parameters, process signatures, and product qualities for AM processes. They emphasized the importance of identifying the correlations between parameters, signatures, and qualities. In Mani *et al.*, AM process parameters are defined as the inputs that are controllable machine parameters and predefined material properties. Process signatures are described as intermediate measurements of AM physics' dynamic characteristics, observable using in-process sensing techniques or derived through analytical simulation and modeling. Product qualities are described as the final state of printed parts, categorized as geometric, mechanical, and physical qualities. The concept of a PSQ framework is insightful and is needed to implement sensing technology, advanced data analytics, and informed adjustment of AM process parameters to characterize, correlate, and control AM processes.

2.2.2 Process parameter optimization in the bioprinting process

A systematic study of the correlations between process parameters and product quality can ensure scalable bioprinting processes [5]. Process parameter optimization in bioprinting is critical to establishing the relationships between printing parameters (e.g., air pressure, print speed, print height, and nozzle design) and the quality of the printed part (e.g., geometric accuracy and mechanical properties). Gleadall *et al.* [6] reviewed how scaffold design parameters, including extruded filaments, laydown patterns, and layer alignment patterns, can affect the mechanical properties of scaffolds and cell biological performance. Kang *et al.* [7] concluded that printing parameters such as pressure, layer height, and path space significantly improve the dimensional accuracy of PEG-DA and gelatin constructs. Kang *et al.* [7] showed that the predicted optimal

values of these printing parameters varied for both materials and performed better than non-optimal parameters in dimensional accuracy. Most of these research efforts emphasized the relationship between printing process parameters and the physical properties of the printed parts without identifying an optimal set of process parameters to achieve desired properties.

The quality of bioprinted parts is highly dependent on material composition and printing process control [8]. However, the current bioprinting practice is to apply a trial-and-error approach using a series of printing process configuration parameters to achieve a high-fidelity print, which is time-consuming and costly [9]. A statistical design approach such as DoE is useful in bioprinting applications for studying the effects of process parameters and their interactions on the quality properties of bioprinted parts [10]. DoE can be used to reduce the number of experimental trials required compared to the typical trial-and-error approach. In previous studies, DoE has been applied throughout the bioprinting process, from material design [11-14] to process parameter optimization [15, 16]. Huber *et al.* [15] applied the Taguchi DoE method to obtain the optimal printing settings for a cellulose gel by correlating pressure and speed with geometry fidelity. Carlier *et al.* [16] used DoE to examine the relationships of deposition temperature, rate, and layer thickness to physical properties for a polylactic acid (PLA) implantable biodevice application. Guerra *et al.* [17] optimized five photocrosslinkable variables for the stereolithography bioprinting process to achieve the desired dimensional accuracy of printed resin components using Taguchi DoE. Gonzalez *et al.* [18] conducted a fractional factorial design and Taguchi study of six process and cell parameters versus the cell survivability rate. Trachtenberg *et al.* [19] employed a full factorial design to optimize propylene fumarate printability by considering the interactions among process parameters, namely, nozzle extrusion pressure, material concentration, travel speed, and filament spacing, versus the material viscosity, filament thickness and pore size. Their work

showed that the extrusion pressure, filament spacing, and nozzle movement speed had the largest effects on the printed pore sizes.

To understand the dynamic bioprinting process, a sensing platform customized for bioprinting is essential to acquire the necessary process data for statistical analysis. In the literature, lacking process sensing tools is identified as limiting the in vivo functionality of bioprinted parts. Precise biomaterial deposition is crucial to determining the success rate of mimicking the heterogeneous structures of native tissues [20]. Wang *et al.* [21] utilized 3D quantification of optical coherence tomography to develop an iterative feedback bioprinting approach to improving the optimal geometric fidelity of cell-laden hydrogel scaffolds. Their work modified the pore size design based on an initial scaffold characterization to meet the target pore size in the second print. Ashley *et al.* [20] used a non-contact 2D laser displacement scanner to enable single-layer material deposition measurement. Their work presented a process measurement and control strategy for single-layer biomaterial extrusion to improve material placement and width.

2.2.3 Thermal and mechanical modeling trend of AM process

The thermal history modeling of AM processes [22] has been studied extensively to understand the dynamic processes underlying the interactions among process parameters, structures, properties, and the quality of AM processes. Selective laser melting (SLM) [23], a process similar to laser welding, uses a laser to melt metals to achieve the goal of geometry build-up. Understanding the thermal distribution history can help prevent defects (such as porosity). On a larger scale, the thermal distribution of a printed part, which is related to the thermomechanical behavior of the molten pool, is the primary factor affecting residual stress formation and microstructure properties [24]. Because of the nature of the layerwise laser heating pattern, the

thermal distributions of printed parts exhibit thermal reheating effects that lead to the cyclical thermal distribution of the process dynamics.

Thermal distribution modeling has been studied numerically and experimentally [24-33]. Korner *et al.* [25] noted the physics involved in melting pool behavior, including melting/solidification, solidification shrinkage, convection, heat conduction, radiation, sintering, gravity, Marangoni convection, capillary forces, vaporization, and laser absorption. Foroozmehr *et al.* [26] developed a 3D finite element simulation for the SLM. This model included the optical penetration depth of the laser in the powder bed. Peyre *et al.* [32] developed a numerical model of the thermal distribution of the laser metal deposition process and validated it using experimental thermal data from thermocouples. Foteinopoulos *et al.* [30] developed a 2D finite-difference model to simulate the thermal history of manufactured parts. The model was used to examine the thermal cycle during the process and was validated by modeling a temperature distribution profile by consecutive layers. Ramano *et al.* [31] presented a thermal model for the laser melting process, including the thermal distribution and melt pool behavior, for titanium, stainless steel, and aluminum materials. Their study concluded that the optimal process parameter sets for maintaining consistent melt pools during the process differ by material type. Promoppatum *et al.* [24] investigated the thermal history of the AM component experimentally and numerically. Peyre *et al.* [32] utilized thermocouples to acquire temperature measurements to validate the thermal predictions of their proposed thermal model. Denlinger *et al.* [33] developed a 3D FEM to predict the temperature, residual, and distortion of a bulk geometry. They found that a newly deposited layer and the layers beneath experienced reheating effects involving residual stress response accumulation in these layers.

Residual stress and distortion formation during metal AM processes can directly influence the mechanical properties of built parts and diminish their structural integrity. Therefore, the ability to predict the development of residual stress and deformation becomes essential to managing the quality assurance of metal AM processes. Existing physics-based predictive models for residual stress and deformation can be categorized into finite element methods (FEM), mesoscopic modeling, and surrogate modeling [34-36]. Most predictive modeling of metal additive manufacturing in this area has been studied using computational techniques such as FEM to handle nonlinearity. Mukherjee *et al.* [36] developed a thermomechanical model to predict residual stresses and distortion. The model utilized heat transfer, fluid flow theory, and the temperature-dependent material properties of Inconel 718 and Ti–6Al–4V. Wangre *et al.* [37] proposed a 3D model for use in investigating thermal behavior and residual stress during selective laser melting of AlSi10Mg. Yang *et al.* [38] implemented a sequential thermomechanical analysis method to predict residual stress and deformation of an LPBF build part.

Another high-fidelity approach described in the literature is the use of mesoscopic-based models incorporating mathematical formulations of complex physical processes, accounting for multiple phenomena caused by fluid dynamics in the melt pool and heat transfer between the interaction of heat source and powder particles [35]. Fergani *et al.* [39] built a novel physics model based on sequential predictions of the temperature profile, the thermal stresses, and the predicted residual stresses. Pal *et al.* [40] developed an integrated 3D dislocation density-based thermomechanical framework using physics-driven coupled multiscale process modeling. Despite the high degree of agreement between the predicted results and experimental data, these FEM-based models are computationally intensive and time-consuming, which could cause difficulty in implementation as part of the rapid quality control system for metal additive manufacturing.

2.2.4 Surrogate modeling need for AM process

Another emerging application of predictive modeling of AM processes is predicting the mechanical properties of built parts from process parameters or/and process signatures acquired from sensing technology. In current industry practices, quality evaluation of mechanical properties is conducted experimentally to ensure quality compliance with stringent standards. However, the time-consuming and costly experimental validation process suggests research opportunities in this field. In literature, Campoli *et al.* [41] utilized FEM to predict the elastic constants, including Young's modulus and Poisson's ratio, of specimens fabricated by SLM. The previously mentioned work by Yang *et al.* [38] extended the kinetics-based model to predict the hardness in an LPBF build by inputting the predicted temperature history. Hayes *et al.* [42] developed a constitutive equation for the yield strength of Ti–6Al–4V specimens fabricated by an electron beam 3D printing process. Similar challenges inherited by FEM-based models or physics-based models present a need for an efficient computational approach. Tapia *et al.* [43] developed a predictive model based on the Gaussian process as a surrogate model to predict the density of metallic specimens fabricated by selective laser melting (SLM). Francis and Bian [44] established a deep learning-based distortion modeling by considering the local heat transfer for pointwise distortion prediction. Mozaffar *et al.* developed a recurrent neural network with a gated recurrent unit (GRU) model to predict thermal histories for various designs and process parameters [45]. Their models accurately predict the thermal history of builds. These works demonstrate a promising direction for the use of surrogate models as an efficient computational approach that utilizes experimental studies and high-fidelity simulation knowledge to correlate process parameters, process signatures, and part qualities.

2.2.5 Inverse design of AM process

In the forward prediction modeling of AM processes, 3D computer simulations study the interaction between processing parameters and the printed parts' thermal behavior [46-48]. However, these computer simulations are associated with a higher computational cost from complex physical models accounting for thermomechanical behavior interaction during printing. Furthermore, the simulation is complicated to reverse modeling for obtaining the optimal parameters inversely. For instance, the simulator is a unidirectional model that yields temperature and mechanical info sequentially but not technically in an inverse form [49]. Besides, the experimental approach of exploring the high-dimensional process parameters design space is also tedious. Many process parameters [49, 50] could influence the process dynamics and the final quality of the printed part. Thus, there lie research opportunities in the inverse design of high-dimensional data of AM processes.

The existing literature on the inverse design is often associated with novel material design discovery, namely porous material design [50], nanophotonic device design [51], composite material design [52], titanium panel [53], and steel material design [54]. For AM processes, the inverse design can be extended to the quality assurance system level, including process parameters optimization and dynamic control at the process level and material design [55]. In general, the inverse design problem optimizes PSQ relationships. The linkage between these three components is often considered an unknown black-box function, where optimization methods are deployed to determine optimal inputs that achieve desired outputs. There are three typical inverse design applications in surveyed literature, including material design, process parameter optimization, and dynamic control at the process level. For instance, inverse problems in materials design are formulated as a parameter–quality optimization challenge. The optimization objective of material

design is to achieve desired quality by optimizing a set of material properties parameters. Another inverse design application can be extended to dynamic control at the process level, utilizing the knowledge of PSQ linkage to inform adaptive control strategies for achieving the desired quality of printed parts. Furthermore, the inverse problems in process parameter optimization involve parameter-quality relationships that explore the optimal set of process parameter solutions that can yield the desired quality, namely mechanical properties, or dimensional accuracy of printed parts.

Inverse design for AM is commonly accomplished using surrogate models with parameter-quality knowledge extracted from statistical models, namely DoE or physics-based simulation, which accounts for process dynamics. The optimal parameter settings can be determined using evolutionary optimization methods and emerging machine learning techniques. A few recent studies have utilized machine learning, namely, artificial neural networks (ANN), deep neural networks (DNN), and active learning (AL), to optimize process parameters for a given desired quality characteristic, as described below.

Researchers have deployed two-step statistical tools, namely, the design of experiments (DOE), to map process parameters with investigated quality characteristics and then perform process parameter optimization using experimental data. For instance, Peng *et al.* [56] applied response surface methodology (RSM) coupled with a fuzzy inference system to optimize the process parameters for desired dimensional accuracy. Raju *et al.* [57] developed a hybrid evolutionary algorithm optimization method. They utilized the Taguchi method to determine the optimal parameter solutions for a printed part's mechanical properties and surface quality. Deswal *et al.* [58] presented multiple approaches that utilize RSM (response surface modeling)–ANN, ANN, and ANN-GA (Genetic algorithm) to correlate and optimize the fused deposition modeling (FDM) process for dimensional accuracy of printed parts. Panda *et al.* [59] demonstrated the usage

of bacterial foraging optimization (BFO) for achieving the desired mechanical properties of the printed part based on central composite design (CCD) to determine FDM parameters. Sood *et al.* [60] applied quantum-behaved particle swarm optimization (QPSO) to achieve the desired compressive strength using face-centered CCD (FCCCD). Mahapatra and Sood [61] determined the optimal process parameters corresponding to the surface roughness of FDM-built parts using the BFO methodology. Rayegani and Onwubolu [62] optimized process parameter settings that yielded optimal tensile strength using group data handling and differential evolution. Rao and Rai [63] demonstrated teaching–learning-based optimization for single-objective and multiple-objective optimization problems in FDM to determine the best process parameter settings in each case study. Mohamed *et al.* [64] utilized a definitive screening design for process characterization and an Artificial neural network (ANN) for process parameters optimization to improve desired creep performance. Saad *et al.* [65] demonstrated an integrated RSM approach and particle swarm optimization (PSO) to achieve the desired flexural strength by optimizing layer thickness, print speed, print temperature, and outer shell speed. Rajpurohit and Dave [66] deployed an adaptive neural network-based Fuzzy Interference System (ANFIS) to correlate between tensile strength and build directions of polylactic acid (PLA) printed parts.

In literature, surrogate-based modeling is emerged to supplement the simulation and experimental approaches to correlate the linkage of process-structure-property-quality for AM processes. Among the surrogate modeling methods, the neural network showed its superior performance in understanding AM processes such as defect detection [67], surface morphology measurement [68], porosity prediction [69], and in-process monitoring and control [70, 71]. Nonetheless, the existing literature lacks uncertainty quantification among neural network architectures. However, these neural networks are deterministic and lack quantifying predictive

uncertainty, which may lead to overfitting issues [72]. Inevitably, uncertainties are present in various stages of AM processes. These uncertainties could be identified from experimental approach, simulation modeling, and surrogate modeling [73] . The detailed sources of uncertainties in AM processes have been reviewed intensively in [74]. Hence, a proper framework of neural network considering uncertainty quantification is crucial to implement for achieving the rapid quality assurance system of AM applications.

2.3 Research gaps analysis

The reviewed literature in Section 2.2.1 has emphasized the need for AM qualification and the fundamental PSQ framework introduced by Mani *et al.* [3] which correlates process parameters, process signatures, and product qualities is essential for establishing the cornerstone of a smart quality assurance system for AM processes. However, there is limited literature expanding on the PSQ framework by further integrating in-process sensing, advanced data analytics, and control adjustments of AM processes.

The related literature review in Section 2.2.2 demonstrated a need for a mathematical approach for bioprinting to correlate process parameter interactions and their effects on desired properties of printed scaffolds. Furthermore, the impact of controllable process parameters on the quality of structural geometry and scaffold properties has not been thoroughly investigated. The existing literature is mainly applied to the material design of the biomanufacturing process and less extended to the process parameter optimization application of bioprinting. In addition, most literature review in Section 2.2.2 is limited to post-process measurement and lacks in-process measurement to acquire multilayer porosity conditions. Hence, characterizing layer porosity during the print is critical for understanding the process dynamics, enabling process parameter optimization to meet the desired porosity quality requirement of the final printed product.

A comprehensive literature review of thermal and mechanical modeling methods for AM processes is presented in Section 2.2.3. However, physical simulation and modeling are limited in that they are time-consuming and computationally costly. Furthermore, little research has focused on data-driven surrogate models for correlating process parameters, thermomechanical behavior, and residual stress distribution. For instance, reheating effects are closely related to the formation of residual stress during AM processes. This creates a need for a data-driven surrogate modeling approach using high-fidelity physics-based modeling that considers process parameters and process signatures to improve the performance of forward prediction problems, as described in Section 2.2.4.

The literature on inverse design applications in AM processes, summarized in Section 2.2.5, focuses primarily on FDM processes and less on metal AM processes due to the extensive requirement of experimental approaches or computer simulations to establish the relationship between process parameters and parts quality. However, these computer simulations are associated with higher costs for computational execution from complex physical models accounting for thermomechanical behaviors during the printing processes. In addition, the experimental approach of exploring the design space of process parameters is tedious because there are many process parameters [105, 106] that could influence the process dynamics and the final quality of the printed part. Thus, research opportunities lie in the inverse design of parameter optimization that is critical for achieving the desired quality of printed parts with better and more reliable performance.

3. Process parameter optimization for layer porosity accuracy of 3D printing polymeric and hydrogel scaffold application

Bio additive manufacturing (bioprinting) technology is a critical emerging field for transforming tissue engineering regenerative medicine (TERM) to produce biological constructs and scaffolds in a layerwise fashion. Geometric accuracy and spatial distribution of scaffold porosity are critical factors associated with the quality of 3D-printed tissue scaffolds. Determining optimal process parameters for tissue scaffold microextrusion 3D printing by traditional trial-and-error approaches is costly, labor-intensive, and time-consuming. In addition, there remains a need for effective in-process sensing techniques capable of observing internal multilayer scaffold structures, such as porosity. Therefore, a DoE-based in-process sensing platform based on integrated light scanning and microscopy was proposed to acquire in-process layer information during the fabrication of polymeric and hydrogel scaffolds. This work implements a customized sensing platform consisting of a 3D scanner and digital microscope for in-process quality monitoring of tissue scaffold biofabrication that provides in situ characterization of each printed layer's geometry condition (e.g., porosity). The proposed sensor-based in-process quality monitoring system can accurately capture layerwise porosity quality. DoE experimental analysis yielded a set of optimal process parameters that significantly improved the geometric accuracy and compressive modulus of thermoplastic- and hydrogel-based tissue scaffolds. The developed sensing system coupled with the DoE approach enables effective process parameter optimization to fabricate porous 3D-printed tissue scaffolds. It can significantly improve the quality and reproducibility of research associated with porous 3D-printed products, such as tissue scaffolds and membranes.

3.1 Introduction

In recent years, 3D bioprinting processes have emerged as computer-aided biofabrication methods for fabricating engineered tissues that support tissue engineering and regenerative medicine (TERM) [75]. 3D printed scaffolds are fabricated as layer-by-layer constructs based on the deposition of thermoplastics or cell-laden hydrogels [76]. Tissues may also be fabricated through the layer-by-layer deposition of thermoplastic and cell-laden hydrogels. The reproducible deposition of 3D-printed construct layers is critical for the resultant tissue quality.

The porosity of a 3D-printed tissue construct plays a significant role in cellular behavior, as well as tissue formation, properties, and function [77-79]. However, 3D-printed tissue scaffolds often exhibit common defects, including voids, overfill, and underfill [67, 80, 81], as illustrated in Figure 3-1, which implies that the process parameters are not optimal. Furthermore, given the inherent process variability of hydrogel dynamics, 3D printing of hydrogel-based tissue scaffolds under non-optimal printing process parameters results in undesirable geometry, affecting cell growth factors [82, 83]. Figure 3-2 shows a porous hydrogel-based tissue scaffold that exhibits poor quality because of non-optimal printing process parameter selection. Furthermore, the need to capture dynamic 3D bioprinting processes for scaffold designs with porous architectures using different materials requires the application of in-process sensing technology. Therefore, it is crucial to leverage sensing technology to capture the scaffold geometry during the dynamic 3D bioprinting process to print complex geometries with high accuracy [21].

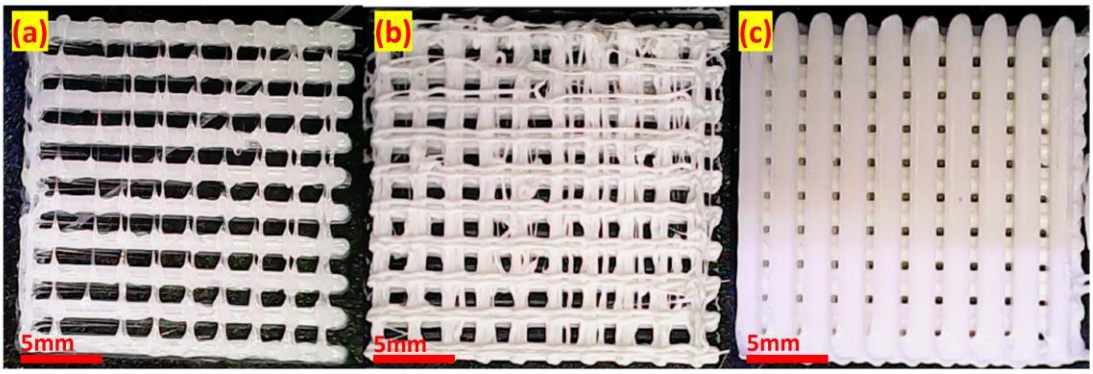

Figure 3-1: Highlights of polymer based tissue scaffold defects (pore structure asymmetry and distribution non-) that occur when the printing parameters are not optimal: (a) Void defect, (b) Under-fill defect, and (c) Over-fill defect.

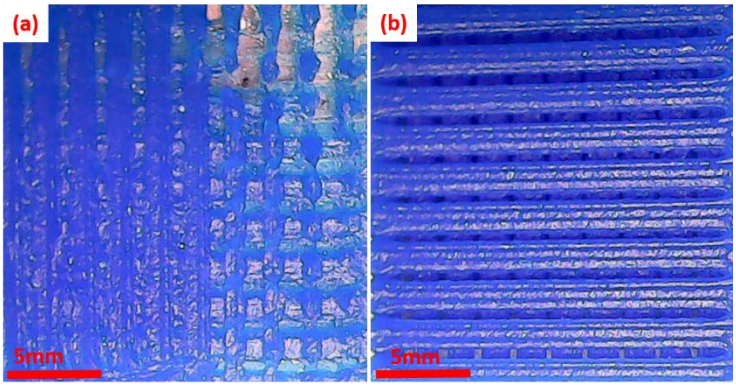

Figure 3-2: Undesired geometry for hydrogel material: (a) incomplete hydrogel material deposition, (b) over-fill defect.

The quality of the layer porosity depends upon process parameters to ensure the geometry accuracy of 3D printed scaffolds [84]. Accurate layer deposition is critical to fabricating the designed geometric structures of hydrogel scaffolds because the geometric cues in tissue-engineered constructs play crucial roles in cell and tissue engineering, including cell maturation, cell differentiation, and tissue regeneration [20]. In addition, deposition defects and inconsistent pore porosity affect the amount of bone growth in bone scaffolds [85]. Hence, the work described in this chapter proposes a sensor-based layerwise porosity monitoring system coupled with DoE to address the above challenges. DoE is a systematic experimental design approach that can be applied to correlating process parameters and the layer porosity of printed scaffolds, significantly

reducing trial-and-error time. The applicability of the proposed method is demonstrated by utilizing experimentally acquired 3D point cloud data and 2D image data from an fused filament fabrication (FFF) platform for bioprinting. The 3D point cloud data and 2D image data provided complementary information regarding the layer porosity quality. The proposed study was accomplished through two major tasks.

(1) A sensor-based in-process monitoring system coupled with a 3D scanner and digital microscope was developed to characterize the layer porosity quality by analyzing high-resolution point cloud data and digital images captured from each layer.

(2) DoE-based process parameter optimization was conducted to identify significant process parameters that affect layer porosity accuracy and determine the optimal process parameter response. The resulting process parameter set was validated through experimental studies to demonstrate the effectiveness of the proposed method.

The remainder of this chapter is organized as follows. The experimental method, in-process sensing platform setup, materials, and data processing procedures, are discussed in Section 3.2. The proposed research framework is presented in Section 3.3. The DoE setup, validation results, and discussion are presented in Section 3.4. Conclusions and future research recommendations are presented in Section 3.5.

3.2 Experimental platform development

The experimental method, including the platform setup, material, and data processing procedures, is presented in detail in this section. First, the in-process sensing platform setup with related machines and sensors is presented in Section 3.2.1. Second, the material and methods related to the scaffold materials, design, print approach, fabrication, and characterization are introduced in Section 3.2.2 until Section 3.2.5. Third, the data processing procedures related to

layer porosity quantification are discussed in Section 3.2.6 and Section 3.2.7. The material testing procedures are described in Section 3.2.8.

3.2.1 In-process sensing platform

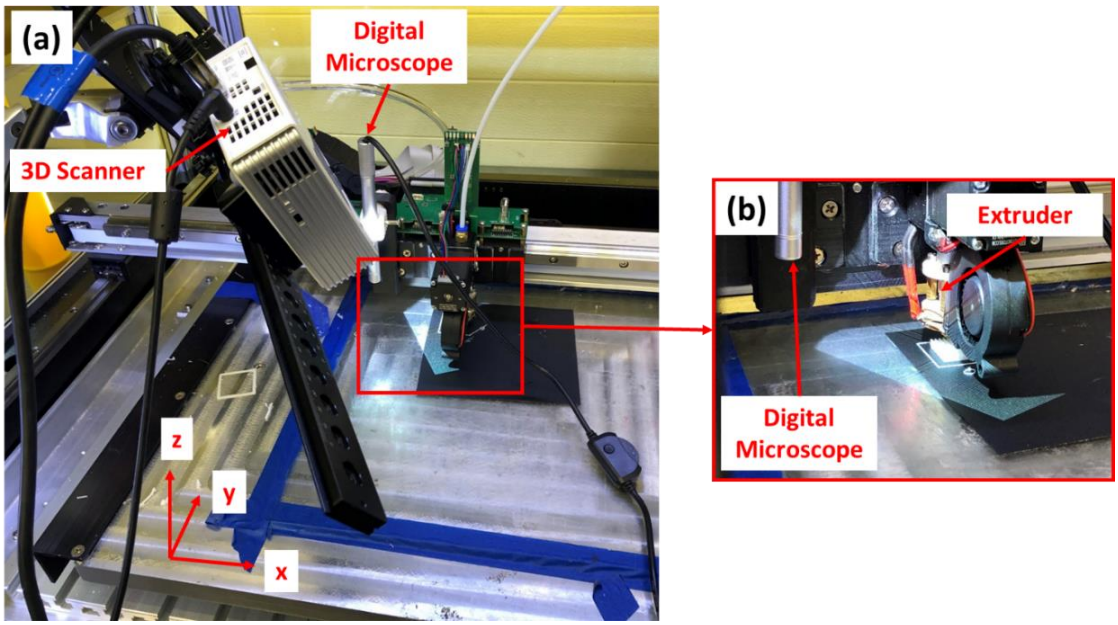

Figure 3-3: Experimental platform with Hyrel System Hydra 460 3D printer for printing the polymeric scaffold: (a) setup with 3D scanner and digital microscope installed to monitor the printed scaffold layer by layer, (b) extrusion system for polymeric scaffold using a heated extruder system.

In this study, an FDM 3D printer, namely a 3D printer (Hyrel System Hydra 640), paired with a 3D scanner (HP 3D Structured Light Scanner Pro S3) and a digital microscope (OPTI-Tekscope OT-V1), as shown in Figure 3-3, were used. The 3D scanner was mounted 45° to the z-plane and 45° to the x-plane to avoid reflection. For high-quality point-cloud data acquisition, the 3D scanner was calibrated to a 73µm/pixel spatial resolution (the average point-to-point distance in the point cloud data) [86]. This spatial resolution was calculated using the field of view (140 × 87.5mm^2) divided by the camera's pixel resolution (1920 × 1200pixels). A digital microscope was installed next to the extruder head in the negative z-plane to capture 2D scaffold surface images from a top-down view. The spatial resolution of the digital microscope, 41.6µm/pixel, was

calculated using the field of view (26.6 × 20mm^2) divided by the microscope's pixel resolution (640 × 480pixels).

Figure 3-4 shows sample data collected from the 3D scanner system. During the data acquisition process, the position of the 3D scanner was fixed to the region of interest on the printed part. The top-view image acquired from the digital microscope was aligned with the 3D point cloud-processed data for geometry verification. A binary image was segmented based on a processed point cloud image with Z-height information to maintain the current layer information. When the printing for each layer is completed, the printing bed is lowered with the digital microscope by the layer height, which is 0.05mm in this experimental setting. The depth of the field is sufficient to capture the surface quality without losing data accuracy. The data processing details for quantifying layer porosity are explained in Section 3.2.6 and Section 3.2.7.

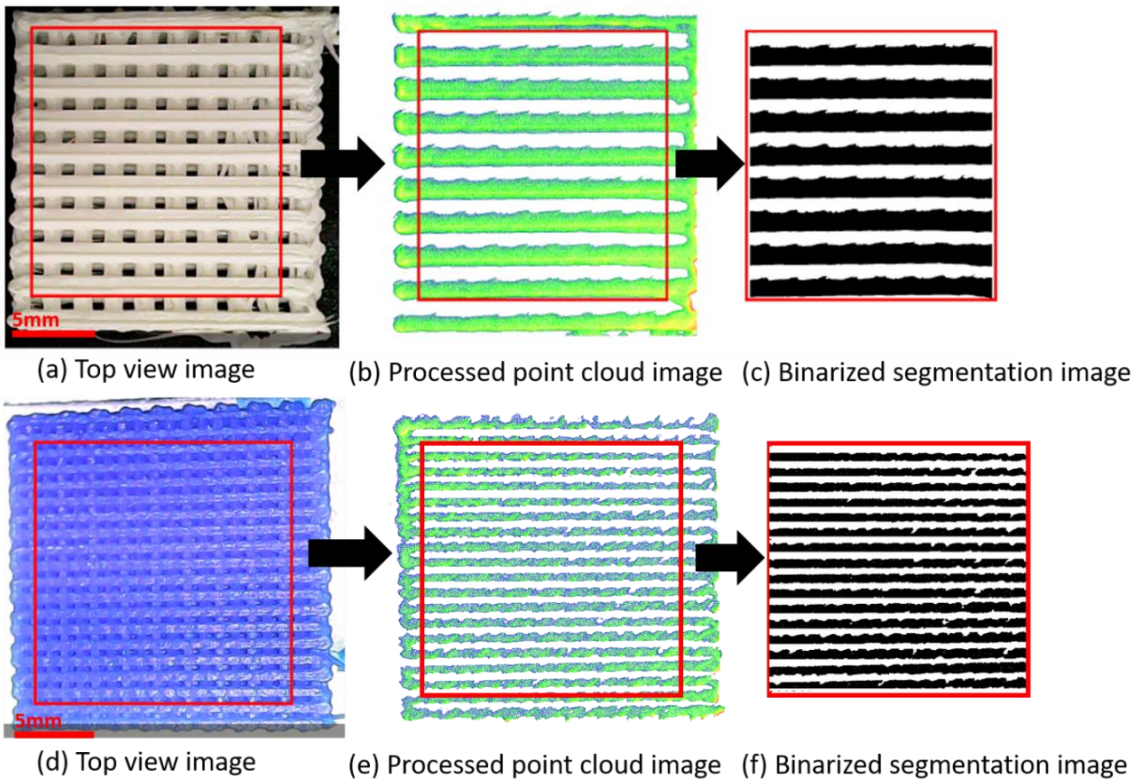

Figure 3-4: A data processing flow from the 3D scanner data acquisition system for PLA (a-c) and Pluronic F127 (d-f): These processed data is for layer 14 of both materials, which the top view image acquired from

the digital microscope (a,d), processed point cloud data of the scaffold surface from the 3D scanner (b,e) and binary segmented image based on point cloud data (c,f).

3.2.2 Scaffold fabrication

This study used two types of scaffold materials: polymeric and hydrogel. The material selected for the polymeric scaffold was polylactic acid (PLA) filament (HATCHBOX, white, diameter 1.75mm), which is a commonly used polymeric scaffold material. The selected hydrogel material was made of Pluronic F127 (Sigma-Aldrich). The hydrogel was mixed with 10% (by weight) cellulose nanofibrils (UMaine PDC) to increase the fluid viscosity and enhance printability [87]. Pluronic F127 hydrogel (30% by weight) was prepared using deionized water, and blue food coloring was added to the hydrogel to decrease the reflectivity of the ink for the 3D scanning process. The ink was mixed for two minutes (Thinky ARE-310) before being transferred to 10 ml syringes to ensure the dispersion of the cellulose nanofibrils and coloring agent.

3.2.3 Scaffold pore size design

This study investigated two scaffold designs to evaluate the general applicability of the proposed method and its performance over two pore size ranges commonly used in 3D bioprinting scaffold design. A 20mm x 20mm x 4mm solid square was designed using AutoCAD software and sliced into two squared pores structures using scafSLICR, an open-source MATLAB-based 3D scaffold slicing algorithm [88]. A pore size of 1mm with 50% layer porosity was selected for polymeric scaffold applications, given the range of common polymeric scaffolds in TERM reported in the literature [14]. For the hydrogel scaffold application, the pore size of 0.5mm with 50% layer porosity was determined based on ranges for typical hydrogel scaffold applications

reported in the literature [18]. Two pore size designs with a layer porosity of 50% are illustrated in Figure 3-5.

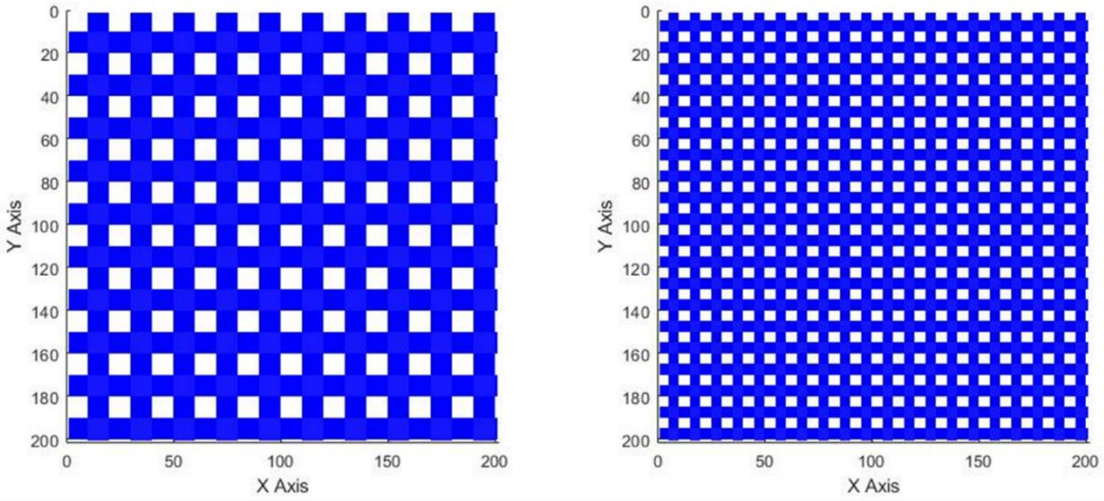

(a) 1-mm pore size, 50% porosity (b) 0.5-mm pore size, 50% porosity

Figure 3-5: Pore size design of printed scaffold: (a) 1-mm pore size with 50% layer porosity for the polymeric-based scaffold, (b) 0.5-mm pore size with 50% layer porosity for the hydrogel-based scaffold.

3.2.4 Scaffold fiber spacing option

The design goal of tissue engineering aims to form pores with spatial control and heterogeneous patterns that can meet different mechanical properties required for the tissue components [88]. Hence, the scaffold fiber spacing is a critical factor in being designed concurrently in XY and Z directions, creating different pore sizes designs. In this study, the scaffold fiber spacing option was chosen as one of the DoE experimental factors, which defines how the scaffold fiber spacing is controlled in the XY and Z directions, as shown in Figure 3-6 (a) and Figure 3-6 (b), respectively. Figure 3-6 (a) demonstrates the scaffold fiber spacing option determined by fiber-fiber spacing in the XY-plane, which is rotated every layer at a 90° angle to create a 0-90 print layout frequently used in the literature [13]. Figure 3-6 (b) and Figure 3-6 (c) illustrate the scaffold fiber spacing option two determined by the fiber-fiber spacing in the Z

direction, repeated at a certain number of horizontal and vertical layouts to create an isometric pore size of 1mm and 0.5mm on XY-plane and Z-plane [14].

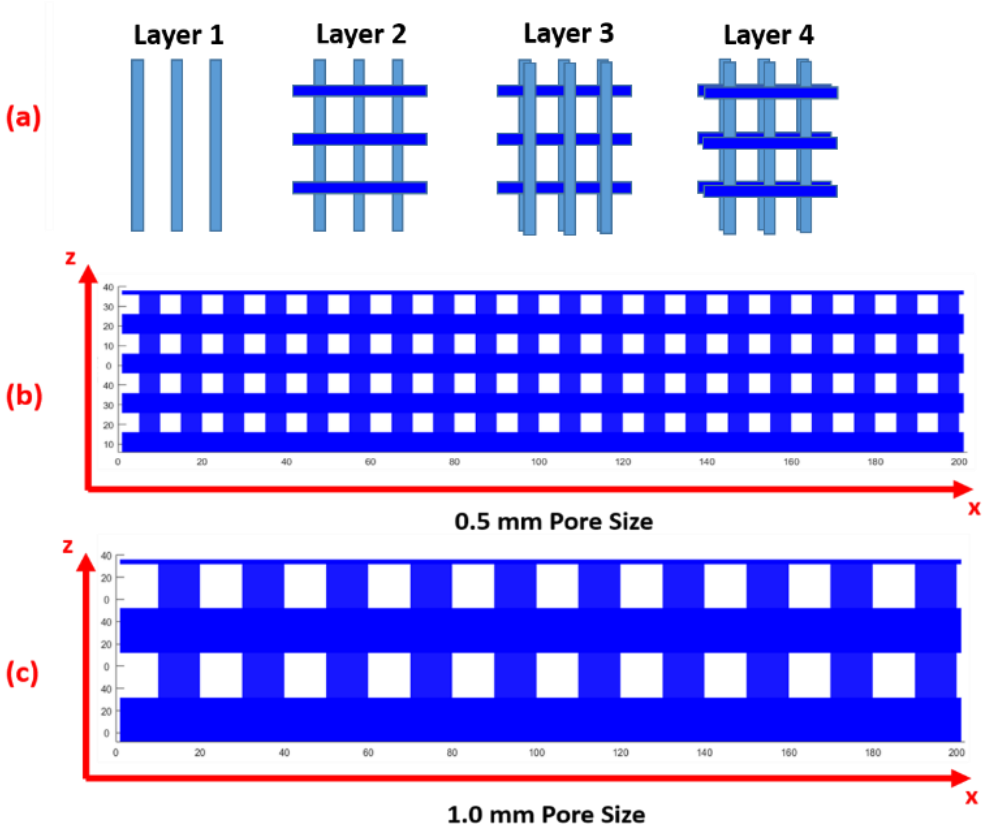

Figure 3-6: The illustration of the scaffold fiber spacing option. a) fiber-fiber spacing in the XY-plane, which is rotated every layer at a 90° angle to create a 0-90 print layout, b) and c) fiber-fiber spacing in the Z direction, which is repeated at a certain number of horizontal and vertical layouts to create an isometric pore size of 0.5mm and 1mm on XY-plane and Z-plane.

3.2.5 Scaffold fabrication

In this study, the industrial FDM printer has versatile material printing abilities and utilized a heated extruder with a 0.5mm nozzle diameter to print 1.75-mm-diameter PLA. This printer can switch the modular extruder heads for different materials. Pluronic-made hydrogels can also be printed using a mechanical-based piston with a standard syringe and 21-gauge syringe needle, as shown in Figure 3-7.

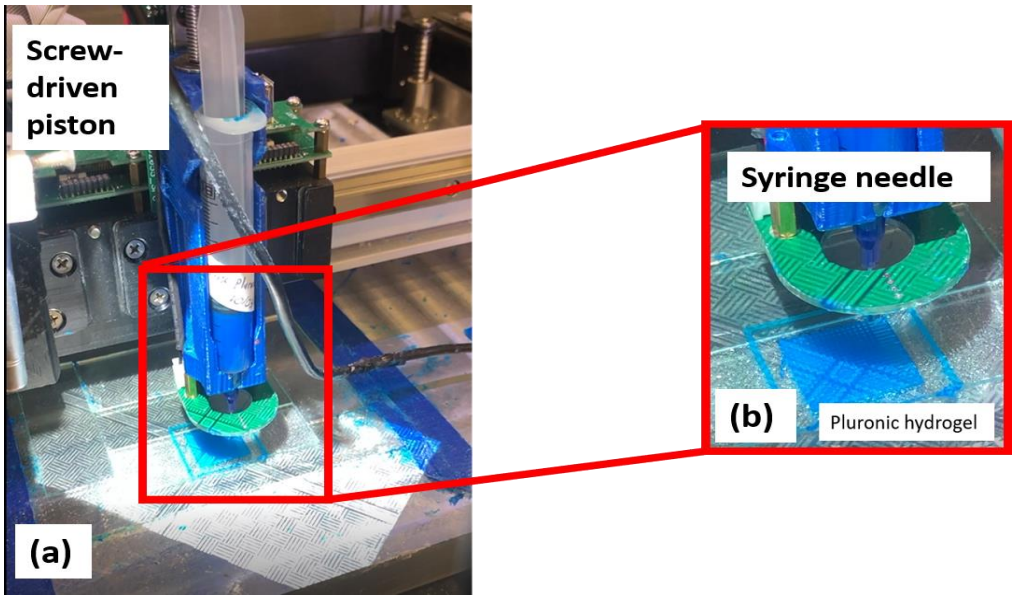

Figure 3-7: The experimental platform for hydrogel scaffold. (a) Overall setup with 3D scanner and digital microscope installed to monitor the printed scaffold layer by layer; (b) the extrusion system for a polymeric scaffold that uses a screw-driven piston and syringe system.

The polymer scaffold was printed using an MK1-250 extruder head and a 0.5 mm extruder nozzle with 210°C nozzle temperature of 50°C substrate temperature within a closed chamber. The filament was heated to 210°C above the PLA melting point. The melted PLA was then extruded onto a heated glass-printing plate through a nozzle. The designed square pore structures were printed layer-by-layer, with 20 layers of each layer height of 0.2mm. The scaffold fabrication procedures were similar to those for the Pluronic hydrogel material, except for the extruder head. This modular SDS-10 extruder is a piston-driven Pluronic F127 hydrogel deposited from a syringe needle.

3.2.6 Data acquisition flow

The printed PLA and Pluronic F127 hydrogel scaffolds were characterized layerwise during the printing process using the customized 3D scanner data acquisition system with the flow described in Figure 3-8. The extruder head is pre-programmed to move sideways and resume printing the next layer after the 40-s pause. Within the pause period, the 3D scanner scans the

scaffold surface for about 30s, and then the digital microscope takes a series of images within 10s. These images were used for the spatial alignment of the processed 3D point cloud data, as described in Section 3.2.7.

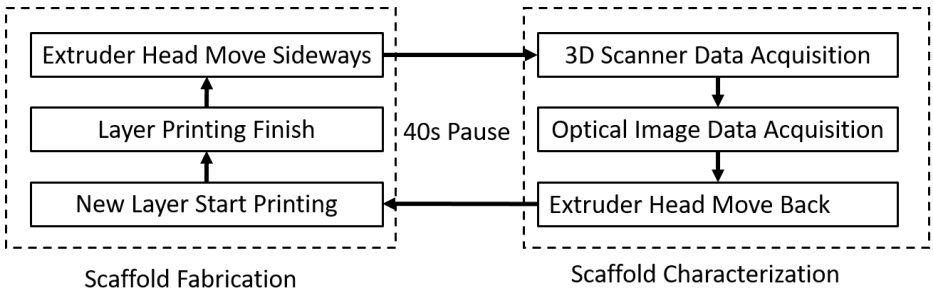

Figure 3-8: Scaffold fabrication and characterization workflow.

3.2.7 Layer porosity quantification

The geometry of the printed scaffold was captured in every layer using the 3D scanner from the experimental platform. The acquired 3D point cloud was then processed offline using CloudCompare (open-source software for processing point cloud data [89] to extract the current layer information for porosity accuracy quantification in the following steps. Because the scanned data is only obtained from one angle and has a blind spot issue, even though it is in 3D, it cannot directly provide the volumetric information for each layer. In a real case study, the edges of the extruded lines are rounded (see blue actual extruded line region in Figure 3-9. Hence, the extruded volume was simplified as the cuboid formed by the red dashed lines in Figure 3-9 [90].

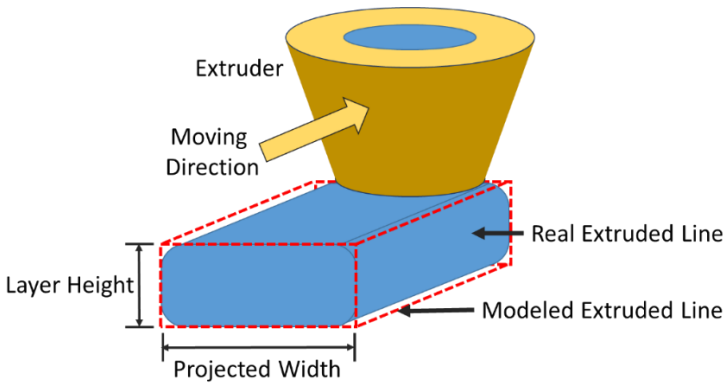

Figure 3-9: Illustration of the volume modeling of the extruded line.

A series of data preprocessing techniques, such as plane transformation [91], region cropping [92], plane fitting [93], cloud to plane distance computation [94], point cloud filtering [95], and point cloud rasterization [89], are applied to transform the raw point cloud into a 2D top view image that was filtered based on the layer height of the printed scaffold. Figure 3-10 shows that the transformed point cloud images were mapped onto the acquired digital images to verify the effectiveness of the point cloud data transformation in terms of geometry and surface information. These 2D point cloud images were processed using ImageJ [96] to binarize the as-printed region of interest (ROI) for layer porosity quantification. A pixel with a value of one was considered part of the material, and a pixel with a value of zero was considered part of the void. The scaffold was designed to have 50% layer porosity. The actual porosity of the printed scaffold within the ROI could be estimated by the total number of pixels in the void over the total number of pixels.

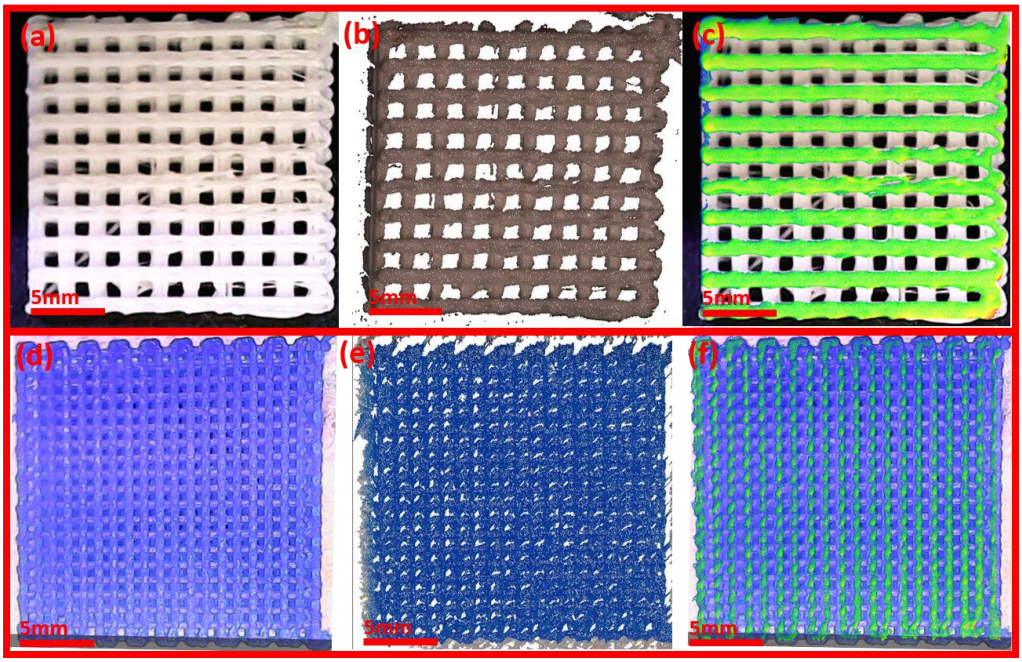

Figure 3-10: (a) (d) The image data of polymer and hydrogel scaffold captured from the digital microscope at layer 14, (b) (e) The raw point cloud data of polymer and hydrogel scaffold acquired by the 3D scanner system at each layer, (c) (f) The transformed point cloud images (color mask) are mapped onto digital images acquired for each layer.

3.2.8 Material testing

Compression tests were performed on PLA scaffold samples (1-mm pore design) under two printing scenarios using optimized process parameter optimization and process parameters set in the DoE trial. Compression testing was performed according to the ASTM D965-15 standard at a 12mm/min deformation rate to 50% strain (KN Instron; 2 kN load cell) machine. The compression modulus of both samples was determined from the slope of the elastic region of the engineering stress-strain curve. The mean ± standard deviation (SD) was used for data expression and analysis. An independent sample t-test was used for compressive modulus studies. The compression tests were repeated three times for each PLA scaffold sample to determine the statistical significance of the compression test results.

3.3 Research methodology

The proposed research framework is summarized in Figure 3-11, which consists of the following three main parts:

(1) In-process sensing platform development for layerwise porosity monitoring: the development of the 3D scanner data acquisition system for the scaffold layer porosity monitoring is presented in Section 3.2.1. The material and methods, including the scaffold design, and fabrication methods, are detailed in Section 3.2.2 until Section 3.2.5. The experimental procedures, including data acquisition flow, layer porosity quantification, and material testing, are detailed in Section 3.2.6 until Section 3.2.8.

(2) Process parameter optimization focuses on the relationship between the layer porosity quality and process parameters. The DoE procedure is established to investigate the relationship between product quality and process parameters in Section 3.3.1. The two-

level full factorial experimental analysis and process parameter optimization are discussed in Section 3.4.1.

(3) Experimental validation studies on the quality performance of the proposed DoE-based process parameter optimization: the DoE validation for layer porosity quantification is verified in Section 3.4.2. The material properties testing results are shown in Section 3.4.3.

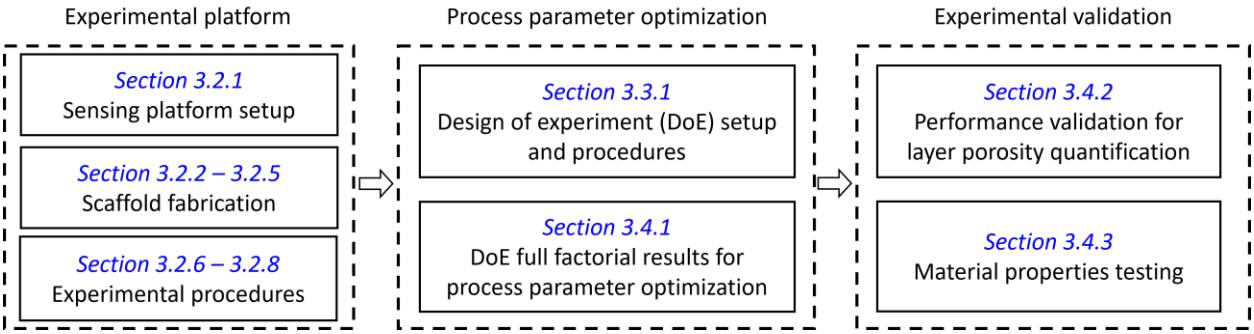

Figure 3-11: The framework of the proposed research approach.

3.3.1 DoE-based process parameter mapping and optimization

A two-level full factorial experimental design was used to investigate the relationship between the desired quality and machine parameters. The results were used to determine appropriate process parameter values.

The two goals of DoE-based process parameter optimization are 1) to minimize the mean error between as-designed layer porosity and as-printed layer porosity estimation and 2) to minimize the standard deviation among all printed layers. Hence, the mean and the standard deviation of layer porosity were selected as the outputs. These two values are calculated by taking the average of all layers based on three replications of DoE experiments. Given the existing literature on process parameters affecting the geometric accuracy of 3D printed scaffolds [67, 96, 97], two machine parameters, including material flow rate (R) and extruder print speed (S) and one design parameter, namely scaffold fiber spacing option, were selected as the factors to carry out the DoE experiments. For the chosen parameters, R refers to the rate at which material was being

extruded through the nozzle; S controls the extruder head print speed and governs the extrusion flow path. The scaffold fiber spacing option determines how the scaffold fiber spacing is controlled on XY-plane and Z-plane. These selected factors may impact the quality of extrusion and thus affect the porosity level during the bioprinting of polymer and hydrogel.

DoE experiments were conducted at two levels of the three process parameters. The ranges of factor levels for flow rate R and print speed S were selected based on experimental trials within the operating range of material printability for both materials, listed in Table 3-1. A 2^3 full factorial experimental design [98] with three replicates was used. A full factorial experiment was chosen in this study to estimate the main and interaction effects with reasonable experimental trials. In addition, the full factorial experiment results can provide process insights into the significance level of those parameters on the statistics of layer porosity quantification. Two experimental tests were performed using polymers and hydrogels, two widely used materials in 3D printed scaffold applications. Hence, 48 DoE experimental runs from two DoE experimental trials were completely randomized to analyze the optimal process parameters for polymer and hydrogel 3D printed scaffolds, respectively.

Table 3-1: The three-factor levels of selected process parameters in two DoE experimental studies.

Material	Pore Size	Scaffold Fiber Spacing	Print Speed	Flow Rate
Polymer	1mm	Option 1	5mm/s	90%
		Option 2	10mm/s	170%
Hydrogel	0.5mm	Option 1	5mm/s	100%
		Option 2	10mm/s	180%

3.4 Case studies

Based on the DoE experimental studies outlined in Section 3.3.1, the two-level DoE full factorial analysis on process parameter significance and process parameter optimization are discussed in Section 3.4.1. Next, the experimental validation studies are performed in Section

3.4.2. Last, the material testing results are detailed in Section 3.4.3 and the results discussion is presented in Section 3.4.4.

3.4.1 DoE full factorial results for process optimization

For the DoE experimental studies investigating both polymers and hydrogels, there were 24 DoE runs for each material. The experimental results from all DoE trials are averaged and tabulated in Table 3-2 and Table 3-3. The experimental results showed the statistics of the porosity estimation at all layers across all runs in one case study. The statistics values shown in both tables were calculated based on the average values of three replications for the same process parameter settings of the DoE experimental study. DoE analysis was performed using Minitab software. The responses of the process parameters were optimized based on the fitted models determined by the significant factors in the DoE analysis. The optimization objectives were to minimize the mean of the porosity quantification error and the standard deviation of the layer porosity estimation. These procedures were performed in the same manner as for the case study of the Pluronic F127 hydrogel.

Table 3-2: Full experimental results for DoE trials of four case studies of the PLA polymer material.

Pore Size	**R1**	**S**	**Scaffold Fiber Spacing**	**Layer Porosity Estimation**	
				Mean	Std. Dev.
1mm	90%	5mm/s	Option 1	55.83	3.48
	90%	10mm/s	Option 1	54.93	3.11
	170%	5mm/s	Option 1	47.02	3.25
	170%	10mm/s	Option 1	47.03	3.72
	90%	5mm/s	Option 2	54.99	3.70
	90%	10mm/s	Option 2	55.77	3.19
	170%	5mm/s	Option 2	30.58	5.12
	170%	10mm/s	Option 2	28.55	5.62

Table 3-3: Full experimental results for DoE trials of four case studies of the Pluronic F127 hydrogel material.

Pore Size	R2	S	Scaffold Fiber Spacing	Layer Porosity Estimation	
				Mean	Std. Dev.
0.5mm	100%	5mm/s	Option 1	54.42	4.73
	100%	10mm/s	Option 1	61.07	5.52
	180%	5mm/s	Option 1	46.17	3.07
	180%	10mm/s	Option 1	40.26	4.33
	100%	5mm/s	Option 2	49.22	6.79
	100%	10mm/s	Option 2	50.60	9.54
	180%	5mm/s	Option 2	36.18	6.30
	180%	10mm/s	Option 2	49.07	7.25

The ANOVA tables [99] show that each best DoE analysis model against the mean and standard deviation of layer porosity was determined based on their significance levels at a p-value less than 0.05. The ANOVA results for the PLA case study in Table 3-4 show that the flow rate R1, scaffold fiber spacing option, and the interaction between the two significantly affected the average layer porosity estimate of the printed scaffold. The ANOVA results for the PLA case study in Table 3-5 show that the flow rate R1**,** scaffold spacing option, and the interaction term between the two significantly affected the standard deviation of the layer porosity estimate of the printed scaffold.

In summary, the flow rate, scaffold fiber spacing option, and the interaction terms between them are significant variables corresponding to the mean and standard deviation of the layer porosity estimation. Furthermore, the print speed (S) was less significant in the polymer [99] case study because the nozzle temperature was kept at 210°C, higher than the PLA melting temperature. This observation agrees with the work reported in [96], which concluded that print speed is less significant in determining the dimensional accuracy of polymer for the FDM process. No further experiments are needed because the lack-of-fit error is insignificant, according to the ANOVA for the PLA polymer scaffold case study.

Table 3-4: ANOVA results for mean layer porosity for PLA polymer scaffold case study.

Analysis of Variance (Mean)

Source	DF	Adj SS	Adj MS	F-Value	P-Value
Model	3	2874.16	958.05	732.36	0.01
Linear	2	2382.44	1191.22	923.04	0.01
Flow Rate	**1**	**1859.54**	**1859.54**	**1440.90**	**0.01**
Option	**1**	**522.90**	**522.90**	**405.18**	**0.01**
2-Way Interactions	1	491.72	491.72	381.01	0.01
Flow Rate*Option	**1**	**491.72**	**491.72**	**381.01**	**0.01**
Error	20	25.81	1.29		
Lack-of-Fit	4	2.43	0.61	0.42	0.79
Pure Error	16	23.38	1.46		
Total	23	2899.97			

Table 3-5: ANOVA results for the standard deviation of layer porosity for the PLA polymer scaffold case study.

Analysis of Variance (Standard Deviation)

Source	DF	Adj SS	Adj MS	F-Value	P-Value
Model	3	13.816	4.6054	4.62	0.01
Linear	2	10.528	5.2638	5.28	0.01
Flow Rate	**1**	**8.375**	**8.3748**	**8.40**	**0.01**
Option	1	2.153	2.1527	2.16	0.16
2-Way Interactions	1	3.289	3.2887	3.30	0.08
Flow Rate*Option	**1**	**3.289**	**3.2887**	**3.30**	**0.08**
Error	20	19.951	0.9975		
Lack-of-Fit	4	4.386	1.0964	1.13	0.378
Pure Error	16	15.565	0.9728		
Total	23	33.767			

As shown in Table 3-6, the ANOVA results for the Pluronic F127 case study show that the flow rate R2, scaffold fiber spacing option, and the interaction term between the two are statistically significant factors that affected the average layer porosity estimation of the printed scaffold. The ANOVA results for the Pluronic F127 case study in Table 3-7 show that the print speed, flow rate, printing direction option, and the interaction between the print speed and the scaffold fiber spacing option are significant variables in the standard deviation of layer porosity estimation. The analysis results reveal that hydrogel material is sensitive to print speed (S), as this variable was statistically significant in the standard deviation of the layer porosity estimation. A significant level of print speed versus geometric fidelity was observed by Ramesh *et al.* [97]. No

further experiments are needed because the lack-of-fit error was found to be insignificant in an ANOVA of the Pluronic F127 hydrogel scaffold case study.

Table 3-6: ANOVA of mean layer porosity for Pluronic F127 hydrogel scaffold case study.

Analysis of Variance (Mean)

Source	DF	Adj SS	Adj MS	F-Value	P-Value
Model	3	1064.24	354.75	26.52	0.01
Linear	2	822.54	411.27	30.75	0.01
Flow Rate	**1**	**799.65**	**799.65**	**59.78**	**0.01**
Option	1	22.89	22.89	1.71	0.21
2-Way Interactions	1	241.70	241.70	18.07	0.01
Flow Rate*Option	**1**	**241.70**	**241.70**	**18.07**	**0.01**
Error	20	267.52	13.38		
Lack-of-Fit	4	70.42	17.61	1.43	0.27
Pure Error	16	197.10	12.32		
Total	23	1331.76			

Table 3-7: ANOVA of mean layer porosity for Pluronic F127 hydrogel scaffold case study.

Analysis of Variance (Standard Variation)

Source	DF	Adj SS	Adj MS	F-Value	P-Value
Model	4	70.573	17.643	13.46	0.01
Linear	3	50.614	16.871	12.87	0.01
Print Speed	**1**	**34.866**	**34.866**	**26.60**	**0.01**
Flow Rate	**1**	**7.092**	**7.092**	**5.41**	**0.03**
Option	**1**	**8.657**	**8.657**	**6.61**	**0.02**
2-Way Interactions	1	19.959	19.959	15.23	0.01
Print Speed*Option	**1**	**19.959**	**19.959**	**15.23**	**0.01**
Error	19	24.900	1.311		
Lack-of-Fit	3	4.465	1.488	1.17	0.35
Pure Error	16	20.435	1.277		
Total	23	95.473			

The step after the process parameter mapping is used to determine the optimal set of process parameters via optimization procedures. The process parameter optimization procedures were implemented using Minitab. Multiple responses with equal weights were optimized to achieve the target layer porosity of 50% and minimize the standard deviation of layer porosity for each case study. The process parameter optimization results are summarized in Table 3-8.

Table 3-8: Process parameter optimization results (layer porosity estimation) for both case studies.

Case Study	*R*	S	Scaffold Fiber Spacing Option
Polymer (1.0 mm)	108%	5mm/s	Option 2
Hydrogel (0.5mm)	143%	5mm/s	Option 1

3.4.2 DoE validation studies results

This section presents the DoE validation studies for two verification scenarios (polymer and hydrogel materials). These two process parameter settings were obtained from DoE analysis based on the experimental results described in Section 3.4.1.

Six validation studies were conducted based on the recommended settings to assess the performance of DoE approaches for optimal process parameters, as summarized in Table 3-8. For each validation case study, three replications were performed to implement the identified process parameter settings from the full factorial DoE analysis. The full validation results, including the statistics of layer porosity estimation, are presented in Table 3-9. The statistics of the layer porosity quantification were calculated based on the average of three replications for each case study.

Table 3-9: The full validation results (layer porosity %) table for both case studies.

Case Study	***R***	**S**	**Scaffold Fiber Spacing**	**Layer Porosity Estimation**	
				Mean	Std. Dev.
PLA Polymer (1.0 mm)	108%	5mm/s	Option 2	50.72	4.25
Pluronic F127 Hydrogel (0.5mm)	142%	5mm/s	Option 1	48.72	2.12

The validation results in Table 3-9 showed that the proposed DoE approaches determine the proper process parameters that yield minimal mean porosity error and minimal deviation error for as-designed 50% porosity (the red line in Figure 3-12) together visualized with the ranges of DoE experimental runs (the blue line in Figure 3-12).

A line plot of layerwise porosity quantification for one set of full factorial experimental and validation studies of the PLA experiment is shown in Figure 3-12. From the line plot, the layer porosity estimation from the validation run achieved an average porosity (the average of all the layers in three replications) of 50.72% closer to the target porosity percentage with a minimum standard deviation of 4.25 (the average of all the layers in three replications).

A line plot of the layerwise porosity quantification for one set of full factorial experimental and validation studies of Pluronic F127 is shown in Figure 3-13. From the line plot, the layer porosity estimation from the validation run achieved an average porosity of 48.72% (the average of all the layers in three replications), closer to the target porosity percentage with a minimum standard deviation of 2.12 (the average of all the layers in three replications). The results demonstrate the successful use of a DoE-based approach to determine the significance of process parameter variables and appropriate process parameter settings for different materials (PLA and Pluronic F127). The validation experiment demonstrated the successful implementation of a design of experiment (DoE)-based in-process sensing platform to improve the geometric accuracy of the layer porosity of scaffolds by meeting the as-designed porosity with less mean error and standard deviation.

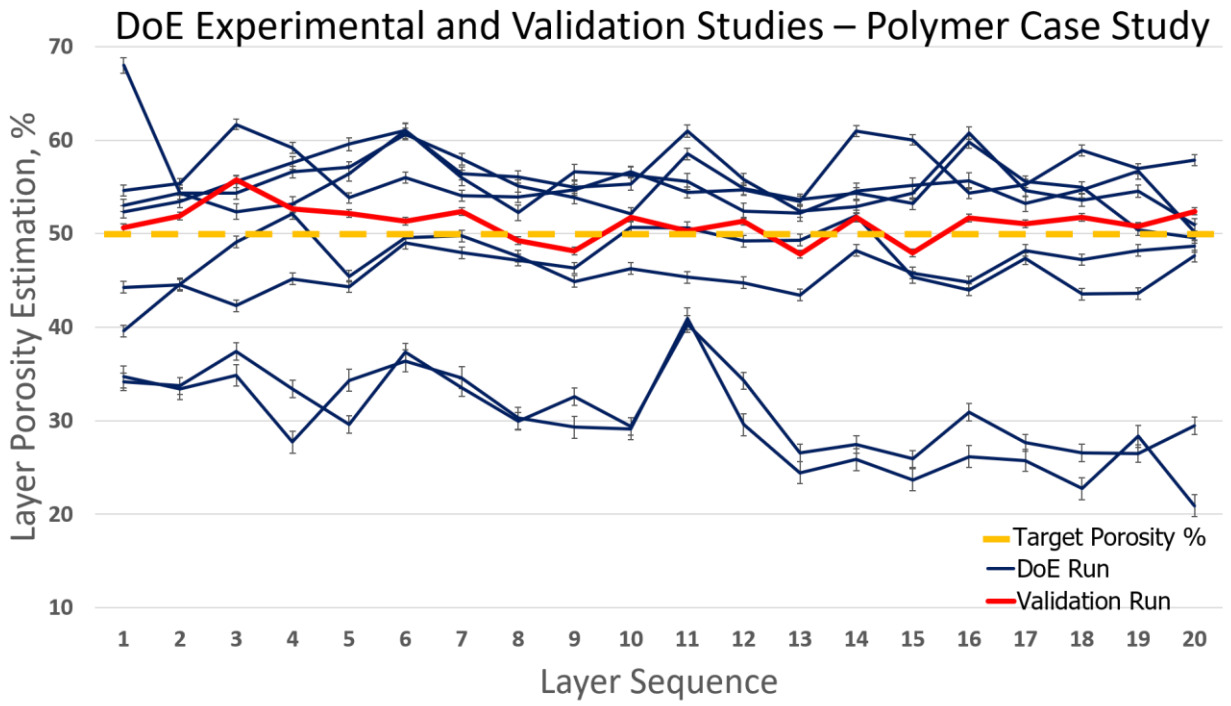

Figure 3-12: Line plot of layerwise porosity estimation for DoE experimental and validation studies for PLA polymer case study.

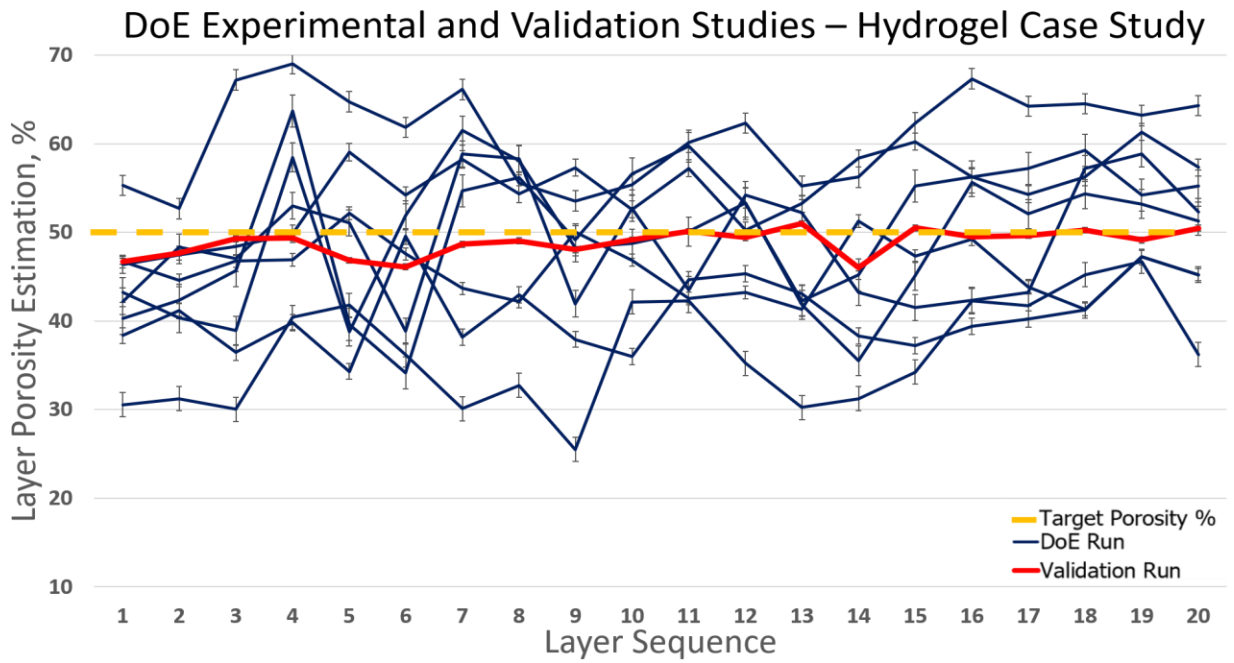

Figure 3-13: Line plot of layerwise porosity estimation for DoE experimental and validation studies for Pluronic F127 hydrogel case study.

3.4.3 Material testing results

The results of mechanical property characterization are presented in Table 3-10. The compressive moduli of PLA scaffolds printed under the two printing scenarios (optimized process parameter vs. DoE trial) were significantly different. The average compressive modulus using the optimized process parameter scenario was 50.36 ±2.79 MPa (n = 3), while the average compressive modulus using the DoE trial process parameter scenario was 34.95 ± 1.37 MPa (n = 3). Both independent sample t-tests of the compressive modulus studies were significantly different at a significance level of $p < 0.05$, as shown in Table 3-11.

Table 3-10: Compressive modulus results for both case studies.

Case Study	Process Parameter	Scaffold Fiber Spacing	Compressive Modulus, MPa				
			T1	T2	T3	Average	Std. Dev
PLA	Optimized	Option 2	49.95	53.96	47.17	50.36	2.79
	DoE Trials	Option 2	33.69	34.32	36.86	34.95	1.37

Table 3-11: Results of sample t-test of compressive modulus studies under two scenarios.

Source	DoE trials	Optimized
Mean	34.96	50.36
Variance	2.82	11.64
Obseravations	3	3
Pool Variance	7.23	
Hypothesized Mean Difference	0	
df	4	
T Stat	-7.01	
P(T<=t) one-tail	0.0011	
t Critical one-tail	2.13	
P(T<=t) two-tail	0.0023	
t Critical two-tail	2.78	

3.4.4 Results discussion

Few studies have been conducted on in-process characterization to capture layer information during the biofabrication of scaffolds. However, the lack of process sensing platforms limits the acquisition of in-process insights of bioprinted parts because precise material deposition is important in the biofabrication of porous constructs (e.g., tissue scaffolds or membranes). Hence, this work demonstrates a customized sensing platform for microextrusion 3D printing processes to acquire the necessary process data for the input and output of the DoE analysis. The proposed sensor-based in-process quality monitoring system can accurately capture layerwise porosity quality.

Research on the systematic study of the relationship between process parameters and product quality is limited in the bioprinting community. Through common trial-and-error approaches, experiments to determine the optimal process parameters for biomaterials are costly, labor-intensive, and time-consuming. This work implements DoE-based process parameter mapping and optimization to utilize the layerwise porosity quality and achieve the desired geometric accuracy with the recommended process parameter settings, resulting in fewer experimental trials. A two-level full factorial covering three factors was designed with 24 trials

conducted for the polymeric and hydrogel scaffolds. The ANOVA helped determine which significant factors, including print speed, flow rate, scaffold spacing option, and the interaction term between them, significantly affected the average and standard deviation of the layer porosity estimation of the printed scaffolds. Furthermore, the proposed DoE approaches recommended an optimal process parameter setting for polymer and hydrogel materials to achieve an as-designed 50% porosity, with an average layer porosity of 50.72 ± 4.25% for PLA material and an average layer porosity of 48.72 ± 2.12% for hydrogel material. Achieving a minimal difference from the as-designed porosity indicates that the proper process parameters determined through the DoE approach meet the geometry design with fewer trials and errors.

In addition, the compression testing results showed that the proposed research framework led to a significant increase in the compression modulus of the printed polymeric scaffolds, as there was a significant difference in the average compressive modulus under the two printing scenarios, including the optimized process parameters and process parameters set in the DoE trials. Meeting geometry design is more efficient with fewer trials and errors, which leads to the desired geometry with improved mechanical properties. In this study, two different scaffold structures with polymeric and hydrogel materials were demonstrated to highlight the general applicability of the proposed research methodology, which can be extended to different bioprinting materials and designs.

Future work will involve extending this process parameter optimization to a bioink-based tissue construct to examine the effect of scaffold porosity variability on biological outcomes (e.g., differentiation outcomes) [100, 101]. Another future direction would extend the current research framework by implementing an in-process monitoring and control strategy to adjust the process parameters during bioprinting. The in-process data acquired at each layer can be utilized using a

data analysis approach to predict the layer quality condition and thus make recommended actions by adjusting the optimal process parameters in real-time.

This work provides a fundamental research framework by establishing a systematic two-step parameter mapping and optimization process to fill the identified research gaps in the bioprinting literature that led to time-consuming bioprinting practice. First, we propose an in-process sensor-based data-acquisition system to measure layerwise quality insights. Second, this work demonstrated a process parameter mapping and optimization strategy to improve the printed scaffolds' geometric accuracy and porosity reproducibility. Under an optimal process parameter, conformance to geometry accuracy and internal scaffold microstructure characteristics, such as porosity, can be ensured, leading to an improved compressive modulus of the 3D-printed porous scaffolds.

3.5 Conclusions and future work

This study successfully implemented a customized sensing data platform coupled with a 3D scanner sensor and digital microscope as an in-process quality monitoring system for 3D printed scaffolds using PLA polymer and Pluronic F-127 hydrogel. This in-process sensing platform enables the layer scaffold quality characterization necessary for the in-situ monitoring of material extrusion conditions during 3D bioprinting processes. The in-process data acquired from the system can estimate layer porosity using point clouds and image post-processing techniques. Furthermore, the layer porosity estimation result is utilized as the output of process parameter optimization to achieve the desired scaffold porosity design with minimal standard deviation.

For case studies, two widely used materials in 3D bioprinting, namely, Pluronic F127 hydrogel and PLA polymer, were used to demonstrate the effectiveness of the proposed in-process sensing system by integrating the acquired layer information into the DoE process. The proposed

DoE-based process parameter optimization was validated by executing the recommended parameter settings. The validation results of both case studies demonstrated that the proposed DoE-based process parameter optimization approach improved the geometric accuracy of the layer porosity of scaffolds by meeting the as-designed porosity with a smaller mean error and standard deviation. With a target porosity design of 50%, the layer porosity estimation of PLA material achieved an average porosity of 50.72% with a minimum standard deviation of 4.25%. The layer porosity estimation of Pluronic F127 achieved an average porosity of 48.72%, with a minimum standard deviation of 2.12%. In addition, the results showed a successful demonstration of DoE-based optimization to determine appropriate process parameter settings for different materials (PLA and Pluronic F127) to achieve minimal error and standard deviation compared to the as-designed porosity quality.

4. Deep-learning-enabled surrogate modeling of process insights associated with metal AM quality for forward prediction problem

Laser powder bed fusion (LPBF) is an AM technique that enables layerwise fabrication of complex objects with material flexibility and waste saving. Because of the labor-intensiveness of existing post-processing metrology assessment and the time-intensive requirement of the AM process simulation, surrogate modeling is essential as a rapid quality inference framework for quality assurance and control. Therefore, deep learning-based surrogate modeling is an emerging research trend that taps into big data that consists of process data and solves the forward prediction problems in AM processes. This chapter presents the high-fidelity AM simulation dataset for developing a deep learning-based surrogate model to predict the final residual stress formation based on high-dimensional thermal history with variations in process parameters. The proposed work develops a deep learning-based surrogate model that considers reheating effects to predict the final residual stress formation based on process parameters and high-dimensional thermal history. It creates a computationally efficient approach for rapid quality assurance of AM processes. The case studies on the high-fidelity AM simulation dataset show that the model can precisely predict the residual stress matrix at each layer by considering reheating effects of thermal cycles and process parameter insights.

4.1 Introduction

Metal AM can produce complex, functional components in small runs at unit costs competitive. However, to realize these potential benefits, research and development are essential in all aspects of production, ranging from a part material property to its dimensional accuracy [102] and surface topography [103]. The applications of AM simulation are emerging as the researchers develop and perform extensive model verification and validation tools. These tools ensure the

analytical accuracy of the simulation results and the reliability of the model predictions to represent the actual process using measured temperature and mechanical properties [49, 104-107].

The attractive feature of using the finite element method (FEM)-based simulation is that the simulator can produce high-fidelity simulation data representing AM processes' actual dynamic process. Though the finite element-based models provide a precise physical understanding of the thermomechanical behavior during the AM processes [108-110], the high computational cost and time inefficiency hurdle its industrial-level implementation for quality assurance (QA) system of metal AM. To overcome these computational cost and time issues, data-driven surrogate models have recently emerged as alternative modeling in metal AM for their low computational cost and better generalization of experimental and simulation results.

Current trends of machine learning applications in AM have led to extensive research in surrogate modeling for establishing a QA framework in the AM community [111, 112]. Data-driven surrogate models have recently emerged for their low computational cost and generalizability of experimental and simulation results [44, 45, 113, 114]. Francis and Bian [44] established a deep learning-based distortion model by considering the local heat transfer for pointwise distortion prediction. Their work demonstrated a distortion prediction within the tolerance limits. Mozaffar *et al.* developed a recurrent neural network with a Gated Recurrent Unit (GRU) model to predict thermal history with various designs and process parameters [45]. Their models accurately predicted the thermal history of the builds.

Establishing the correlation among process parameters, process signature, and product qualities in AM process is critical in the QA system of metal AM to achieve high-quality additive manufactured parts [1]. Remarkably, the reheating effects of thermal cycles contribute to residual stress formation that could affect the functionality of printed parts [115-117]. However, most

surrogate models only considered limited process parameter ranges and did not account for the reheating effects of thermal cycles in their modeling. There remains a lack of literature exploring surrogate models for correlating thermomechanical behavior and residual stress distribution. Therefore, we present a deep neural network-based framework for predicting residual stress of laser powder bed fusion (LPBF) under different parameter settings using thermal histories with reheating effects extracted from FEM.

Thus, this chapter presents a need for a data-driven surrogate modeling approach using the high fidelity of physics-based modeling. In summary, a data-driven surrogate model with the ability to integrate knowledge across process parameters, thermomechanical behavior, microstructure, residual stress, distortion understanding, and mechanical responses is highly desired for the imminent implementation of the quality assurance system of metal AM. In addition, the proposed approach is promising with the ability to integrate knowledge from process parameters and thermomechanical behavior for the promising implementation of the QA system of metal AM.

4.2 Theoretical background

The effects of process parameters and thermal reheating cycles on residual stress are briefly described in Section 4.2.1. The theoretical background of thermal and mechanical modeling is summarized in Section 4.2.2. An explanation of how AM simulation works based on physics-driven theories is presented in Section 4.2.3.

4.2.1 Process parameter and thermal reheating effects on residual stress formation

Residual stress formation during metal AM processes occurs as a result of complex thermal phenomena arising from the thermal reheating effects of the localized heat source. The heat source, i.e., laser beam, rapidly heats the surface at the top layer and subsequently fully or partially reheats

the already solidified layers underneath. As a result of this heat source reheating effects, large temperature gradients occur in the applied heated area due to the high energy density heat input that leads to the effect of non-uniform thermal expansions and contractions [118]. These thermal fluctuations would repeatedly occur when increasing layer deposition and result in the accumulation of the residual stress in the additive printed part. In the end, the residual stress formation is not desired in most AM cases as these may lead to the severe consequence of build part failures that are subjected to other undesirable outcomes, including displacement, cracking, poor surface quality, and weakened fatigue performance [119].

Given the significant impact of mechanical responses on the quality of printed AM parts, many studies have suggested that process parameters influence the residual stress [120, 121] and microstructure formation during AM processes [122, 123]. Investigating the correlation between process parameters and residual stresses, both experimental approaches and numerical simulation are thoroughly studied in these literature works [104, 121, 124-126]. Furthermore, these thermal-related insights, particularly thermal reheating cycles, affect AM-built parts' microstructure and mechanical properties. For instance, Rodrigues *et al.* showcased that the microstructure and mechanical properties of HSLA steel parts are correlated with the thermal cycles involved in the wire and arc additive manufacturing process [116].

The literature shows that process parameters and thermal reheating histories are key factors influencing residual stress in additive built parts. Therefore, thermomechanical models for simulating the metal AM process, including laser powder bed fusion (LPBF), offer insights into surrogate modeling for building and using data-driven smart quality assurance systems for AM systems that can relate process parameters, process signatures, and product qualities.

4.2.2 Thermal model

The simulation data for this research task was acquired using Autodesk Netfabb Local Simulation, a Newton–Raphson-based nonlinear finite element model (FEM) [104]. The goal of the AM simulation was to simulate the thermomechanical behavior of AM processes. The thermomechanical FEM model is based on the thermoelastoplastic constitutive material model [49]. Therefore, the sequential thermomechanical modeling approach yields unique characteristics, which both thermal and mechanical analysis can be extracted separately from simulation modeling. Hence, both simulation data can be served as input and output of the machine learning model given the same spatial and temporal resolutions. Figure 4-1 illustrates the framework of physics-based simulation, which comprises three components: model inputs, FEM model, and model outputs. Material properties and process parameters are model inputs to simulate the temperature of the part on a temporal and spatial scale. Next, the thermal model simulates the thermal loads, and the simulated temperature insight is fed into the mechanical model. The mechanical model yields the simulated part qualities, including stress, strain, and displacement during the build process.

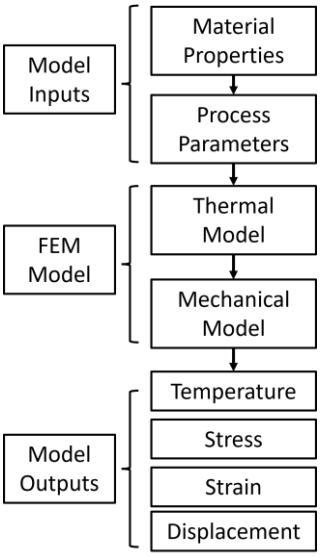

Figure 4-1: A framework of physics-based simulation consisting of model inputs, FEM model, and model outputs.

The thermal modeling of FEM simulation involves thermal equilibrium, which is governed by a set of thermal equations, including the heat source model, boundary condition, and boundary heat losses. These governing equations are required to generate the metal AM processes' thermal field throughout the history of the simulation process. Hence, the thermal model's outputs are temperature history, temperature gradient, heat flux, and interlayer temperature. Following [33], the simulation applies a weakly coupled modeling approach known as the Galerkin approach. The simulation results from the thermal analysis are then fed into the mechanical analysis. Figure 4-2 describes the thermal equilibrium's critical governed thermal equations, including the heat source model, boundary condition, and boundary heat losses.

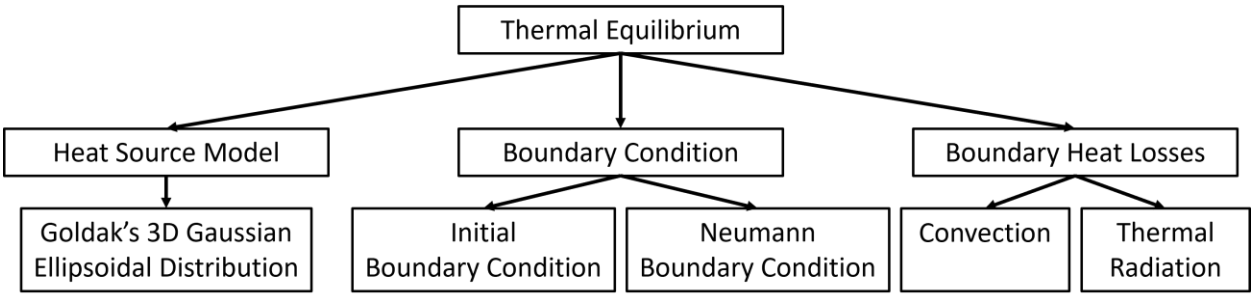

Figure 4-2: The governing thermal equilibrium equations, including heat source model, boundary condition, and boundary heat losses.

The following paragraphs describe the governing thermal modeling used by Autodesk Netfabb Local Simulation, which explains how thermomechanical modeling generates the necessary dataset for machine learning-based modeling [127]. First, the thermal equilibrium for FEM simulation of AM process can be written as the following equation:

$$\rho C_p \frac{dT}{dt} = - \frac{\partial (q_i(x_j, t))}{\partial x_i} + Q(x_j, t) \quad (1)$$

where ρ is the constant density of a body, C_p is the isotropic specific heat capacity of a body, T is the temperature, t is the time, q_i is the local heat flux through the part, x_i and x_j are the location

vectors, respectively, and Q is the heat source model. Furthermore, the local heat flux vector can be expanded by using Fourier's conduction equation that describes the distribution of heat through the part:

$$q_i = -k(T)\,\frac{\partial T}{\partial \mathrm{x_i}} \tag{2}$$

where k(T) is the material's thermal conductivity, which is dependent on the isotropic temperature, and $\frac{\partial T}{\partial \mathrm{x_i}}$ is the thermal gradient that reflects how temperature changes with location.

Two boundary condition assumptions are made for the thermal modeling. The first assumption is that a Neumann boundary condition is considered to provide an equation for the boundary node. Under the Neumann boundary condition, the value of the gradient of the dependent variable is prescribed on the boundary [128]. The second assumption is that the initial condition assumes the initial temperature, T_0 is equivalent to the ambient temperature or preheating temperature of build plate, T_∞. For subsequent time steps, the initial condition of the temperature is updated to the nodal temperatures calculated at the previous time step.

Third, the heat source of metal AM is typically from the laser beam or electron beam. There are two heat input models for AM process simulation: 2D heat flux or a 3D body heat source distribution. The simulation applies the commonly used Goldak's 3D Gaussian ellipsoidal distribution heat source model [106]:

$$Q = \frac{6\sqrt{3}P\eta}{abc\sqrt{\pi}}\,exp\left(-\frac{3x^2}{a^2}-\frac{3y^2}{b^2}-\frac{3(z+v_s t)^2}{c^2}\right) \tag{3}$$

where P is the heat source power; η is the absorption efficiency; a, b, and c are the width, depth, and length of the ellipsoid, respectively; x, y, and z are the local coordinates of the moving heat source; v_s is the travel speed of the heat source; and t is the time.

Fourth, another essential consideration for the simulation of thermal modeling is boundary heat losses that may occur during AM process in different forms. The governed boundary heat loss due to free convection, forced convection, and thermal radiation can be written as follows:

$$q_{conv} = h(T_s - T_\infty) \tag{4}$$

$$h = h_{free} + h_{force} + h_{rad}) \tag{5}$$

where q_{conv} is the total convective heat flux, h is the sum of the heat transfer coefficient of free convection (h_{free}), forced convection (h_{force}), and linearized thermal radiation (h_{rad}), T_{s} is the temperature at the surface, and T_∞ is the ambient temperature.

4.2.3 Mechanical model

Since the simulation is sequential, mechanical modeling uses the previously generated thermal history across each node to calculate each step's mechanical responses. Figure 4-3 summarizes the mechanical model's governed quasi-static stress equilibrium cases with associated equations. The Autodesk Netfabb Local Simulation implements these mechanical-related equations to demonstrate how the thermomechanical model simulates mechanical responses. In addition, the outputs of the mechanical model are stress-related properties (von misses stress, principal stress, and Cauchy stress), strain-related properties (plastic and elastic strain), and location-related properties (displacement).

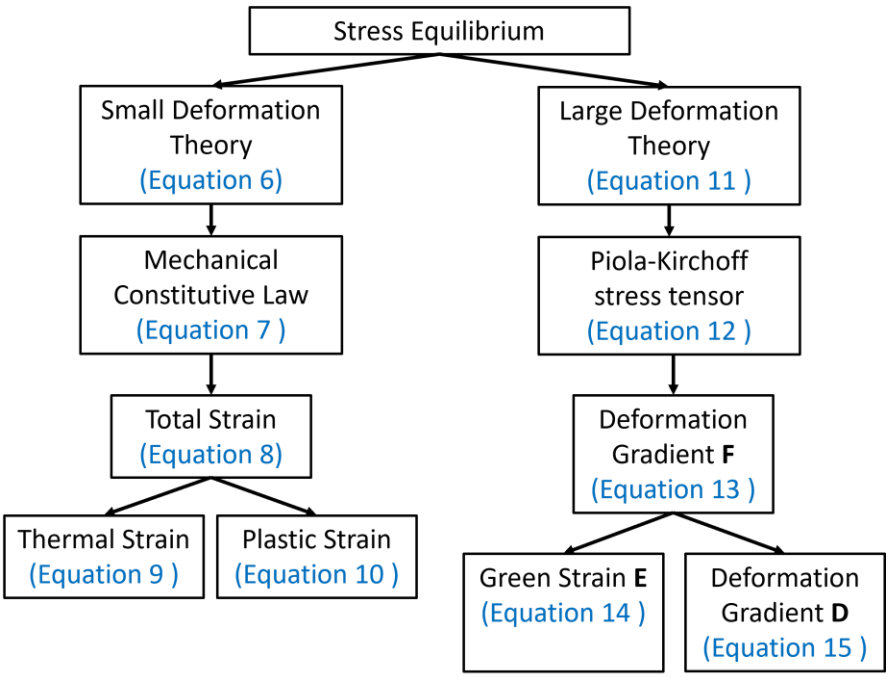

Figure 4-3: The governing quasi-static stress equilibrium cases with associated equations in the FEM software.

There are two mechanical model cases considering small deformation and large deformation. For the first case considering small deformation, the governing stress equilibrium equation is written as follows:

$$\nabla \cdot \sigma = 0 \tag{6}$$

where σ is the stress.

The generalized Hooke's law, sometimes called the constitutive law, is required to relate the relationships among strain, stress, and material properties, which can be written in the following form:

$$\sigma = C\epsilon_e \tag{7}$$

where C is the symmetric fourth-order material stiffness tensor, and ε_e is the elastic strain tensor.

In a small-deformation case, the elastic strain can be related to the total strain, which can be written as follows:

$$\epsilon = \epsilon_e + \epsilon_p + \epsilon_T \tag{8}$$

$$\epsilon_e = \epsilon + \epsilon_p + \epsilon_T$$

where ϵ is the total strain, ϵ_e is the elastic strain, ϵ_p is the plastic strain, and ϵ_T is the thermal strain.

The thermal strain, the strain that forms during the heating and cooling phase of AM process, can be written in the following form:

$$\epsilon_T = \alpha \, \Delta T \tag{9}$$

where α is the coefficient of thermal expansion and ΔT is the algebraic change in temperature.

The plastic strain is defined as permanent deformation occurred when the material is loaded beyond its elastic limit. The plastic strain can be calculated by applying the von Mises yield criterion and the Prandtl-Reuss flow rule, which can be formulated as follows:

$$f = \sigma_m - \sigma_y(\epsilon_q, T) \leq 0 \tag{10}$$

$$\dot{\epsilon}_p = \dot{\epsilon}_q a$$

$$a = \left(\frac{\partial f}{\partial \sigma}\right)^T$$

where f is the yield function, σ_m is von Mises stress, σ_y is the yield stress, $\dot{\epsilon}_q$ is the equivalent plastic strain, and a is the flow vector.

For the second case of large deformation, the large deformation theory is accounted for the current spatial location experiencing unusual changes from its initial reference. In the case of a large deformation scenario, the governed stress equilibrium equation is different from the small deformation scenario. The governing stress equilibrium for a large deformation scenario is written as follows:

$$\nabla_x \cdot \mathbf{P} = 0 \tag{11}$$

where ∇_x is the algebraic deformation change in part x and P is the first Piola-Kirchoff stress tensor **P** which can be written as follows:

$$\mathbf{P} = J\sigma \cdot F^{-T} \tag{12}$$

where σ is the stress tensor and J is the determinant of the deformation gradient F, which is written as follows:

$$\mathbf{F} = \frac{dx}{d\mathbf{X}} \tag{13}$$

The deformation gradient F can be related to displacement gradient D, and the Green Strain E is written as follows:

$$\mathbf{E} = \frac{1}{2}(D + D^T) + \frac{1}{2}D \cdot D^T \tag{14}$$

$$D = \boldsymbol{F} - \mathbf{I} \tag{15}$$

where E is the Green strain, D is the deformation gradient D, and I is the identity matrix.

4.3 Research methodology

Process parameters, thermal histories, and mechanical responses are closely related and interconnected through governed equations, given the dynamic physics-based theories behind thermal and mechanical modeling. The relationships among them are highly non-linear, and the data inherited by these parameters, signatures, and qualities in AM process is high-dimensional. In addition, a surrogate-based model is well fit for high-dimensional data and non-linear relationship modeling. Hence, a surrogate-based approach can be utilized to model thermal and mechanical modeling in a data-driven approach by feeding the model with physics-driven data input and output.

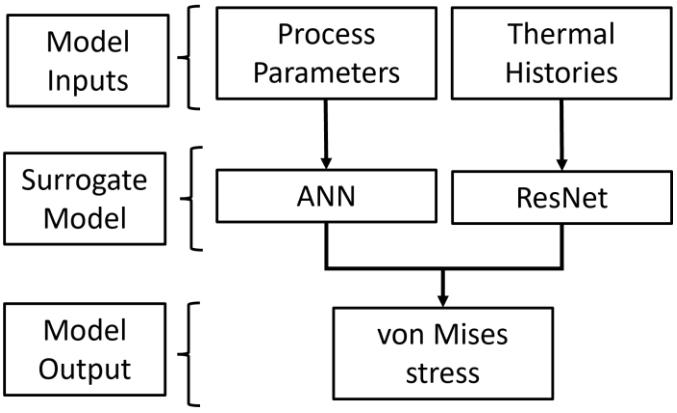

Figure 4-4: A machine learning-based surrogate model framework that integrates process parameters and thermal histories onto ANN and ResNet to predict von Mises stress of printed parts.

Inspired by the convolutional neural network (CNN) and artificial neural network (ANN), a machine learning-based surrogate model is proposed to correlate process parameters and signatures with parts qualities. Similar to the physics-based modeling components shown in Figure 4-1, the proposed machine learning-based surrogate does take model inputs to correlate with model outputs. However, one major difference between physics-based simulation and surrogate-based modeling is that the proposed machine learning-based surrogate model incorporates a deep neural network for predicting residual stress from the reheating effects of the thermal history of metal AM processes and process parameters. Both ANN and CNN architectures are utilized to create surrogate modeling that learns the non-linear correlation relationships of governed equations presented in thermal and mechanical modeling. Therefore, a machine learning-based surrogate model framework can be illustrated under the ANN and CNN model architecture ensemble, as shown in Figure 4-4.

4.3.1 ResNet-ANN-Re model architecture

Figure 4-5 shows that the ResNet-ANN-Re model is proposed by taking layer-wise thermal histories with reheating effects to undergo a customized ResNet architecture. In addition, the proposed model considers process parameters, including laser speed, laser power, and hatch

spacing, by using an artificial neural network (ANN), as illustrated in Figure 4-5 (b). The four fully connected layers are utilized to extract the feature of process parameters. ResNet features are flattened and concatenated with ANN, and these are passed through a fully connected layer with the final regression layer to predict the residual stress. The model parameters are determined by grid search-based hyperparameter tuning. The model is trained using the mean squared error loss function between predicted and simulated residual stress.

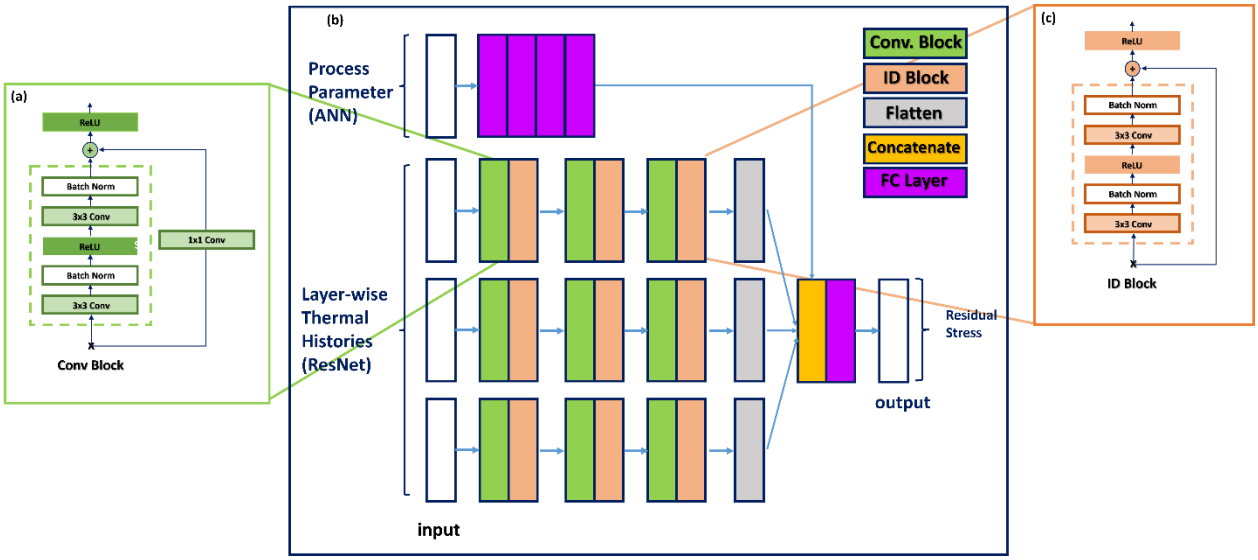

Figure 4-5: The overview of deep neural network architecture for the forward prediction modeling. a) Convolutional block, b) ResNet-ANN model architecture, c) identity block.

The advantage of AM simulation is its capability to extract thermal histories underneath layers known as reheating effects. Therefore, the convolutional neural network module with a ResNet backbone is adapted to account for the reheating effects, which involves high dimensional spatial-temporal thermal data. This deeper neural network applies residual connections as a shortcut over the convolutional layer to resolve the vanishing gradient problem [129]. The convolution and identity block mechanisms are illustrated in Figure 4-5 (a) and Figure 4-5 (c). The deep residual network of convolution layers can learn various low, mid, and high-level features in the data. Hence, the residual connection is a simple yet powerful design that enables deeper neural

networks without risking performance degradation. Thus, ResNet is selected for high dimensional data like FEM simulation data that can accelerate the speed of neural network training by having a smaller number of weights relative to the network depth.

4.3.2 Dataset curation

The training dataset is acquired using Autodesk Netfabb Local Simulation, a Newton–Raphson-based nonlinear FEM solver [104] as detailed in Section 4.2.1 and Section 4.2.2. The simulation software theoretically converts the governing physics equation to a weak formulation, assuming the one-way relationship between thermal and mechanical behaviors [49]. This sequential thermomechanical modeling yields thermal and mechanical analysis that can be extracted separately for the input and output of the proposed model.

For the data curation of this work, Ti-6Al-4V alloy material is selected with three significant process parameters, including laser scan speed (200mm/s-1200 mm/s), laser power (50W-350W), and hatch spacing (0.08mm-0.18mm). The ranges of these process parameters are chosen to create a more extensive dataset covering the typical range of metal AM processes in the literature [49, 104]. The selected part design is a cuboid of 1mm × 1mm × 0.15mm (3-layer height). There are 27 data samples for model training, validation, and testing purposes. The visualization of thermal distribution followed by the moving laser source is illustrated in Figure 4-6 (a), while the residual stress after printing is visualized in Figure 4-6 (b).

Given that the thermal history of the bottom layers is impacted by the reheating [116, 117], these layers carry information about the reheating effect. Figure 4-6 (c) illustrates the case where reheating is not considered (we have only included the thermal data at the top layers). In contrast, Figure 4-6 (d) shows the case where the reheating effect is considered by including the thermal

data at the top layers and the thermal data from all the bottom layers. The thermal histories of the bottom layers are updated due to the reheating effects.

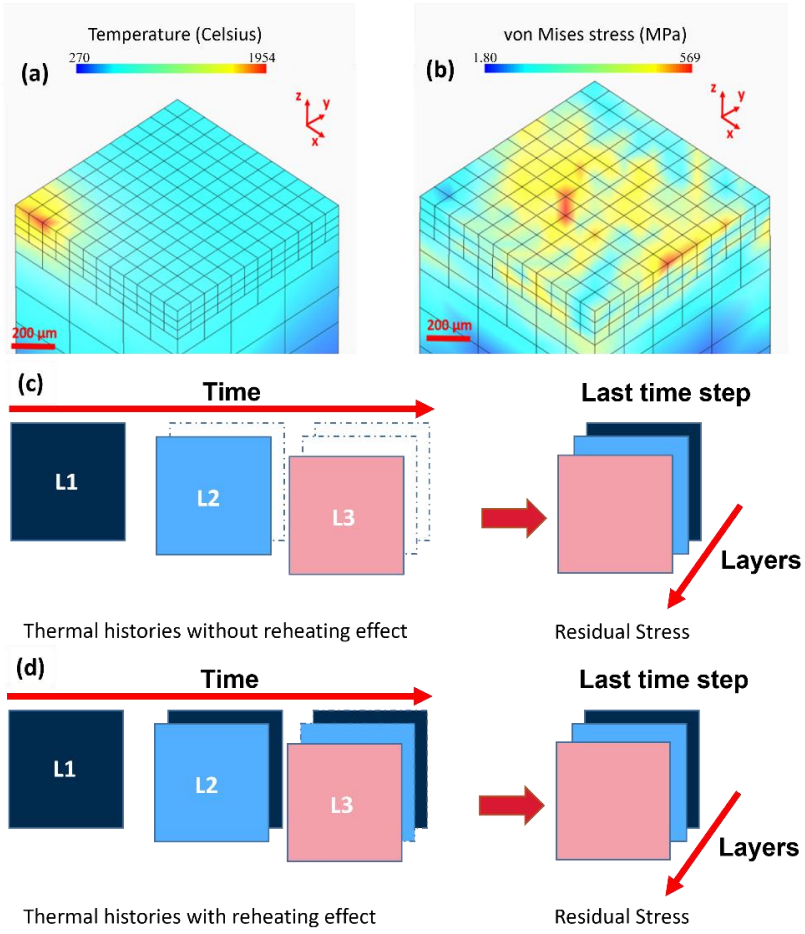

Figure 4-6: (a) FEM simulation results of fine-scale temperature distribution with moving laser source; (b) residual stress at final time step with 200mm/s laser scan speed, 50W power, and 100µm laser spot; (c) the case where reheating is not considered (only considered thermal histories at each top layers); (d) the case where reheating is considered by including thermal histories at each top layers as well as thermal histories from all bottom layers.

4.3.3 Proposed model setup

The proposed ResNet-ANN-Re model is trained using two NVIDIA GeForce RTX 2080 Ti GPUs and TensorFlow Keras library [130]. The input is layerwise thermal histories, and the output is layerwise residual stress at the final time. All inputs and outputs are normalized using a min-max normalization method ranging from 0 to 1 [131]. The dataset is split between training

(18 samples), validation (5 samples), and testing (4 samples). The hyperparameter tuning is optimized by the grid search cross-validation method. The final models are completed within 18 hours using an Adam optimizer [132] with a learning rate of 0.0005, a batch size of 4, and 700 epochs [133].

4.4 Results and discussions

The proposed model is validated under three case studies to evaluate the effects of process parameters and reheating effects against the model prediction performance. Three models, including ResNet, ResNet-ANN, and ResNet-ANN-Re (proposed), are categorized by whether process parameters and reheating effects are considered. ResNet is base architecture without process parameters and reheating effects. In addition, the ResNet-ANN model considers only process parameters. The proposed ResNet-ANN-Re model considers both parameters and reheating effects. The performance of the three models is shown in Table 4-1. The correlation, mean square error (MSE) and mean relative error (MRE) for the ResNet architecture are 0.773, 0.000215, and 1.04%, respectively. The correlation, MSE, and MRE for the ResNet-ANN model are 0.788, 0.000178, and 0.99%, indicating that the performance of a model with an ANN structure to account for process parameters is better than that of a model without such a structure.

Table 4-1: The result of the deep neural network model for correlation, mean square error, and mean relative error percentage for all models.

Model	Process Parameter	Reheating Effects	Correlation	MSE	MRE (%)
ResNet	No	No	0.773	0.000215	1.04
ResNet-ANN	Yes	No	0.788	0.000178	0.99
ResNet-ANN-Re (proposed)	**Yes**	**Yes**	**0.814**	**0.000158**	**0.94**

The proposed ResNet-ANN-Re model achieves the best performance with 0.814 correlation, 0.000158 MSE, and 0.94% MRE. The correlation between predicted and simulated

residual stress by three models is illustrated in Figure 4-7. The result shows that the proposed model considering process parameter insights and reheating effects can accurately predict and capture the trend between predicted and simulated residual stress of LBPF.

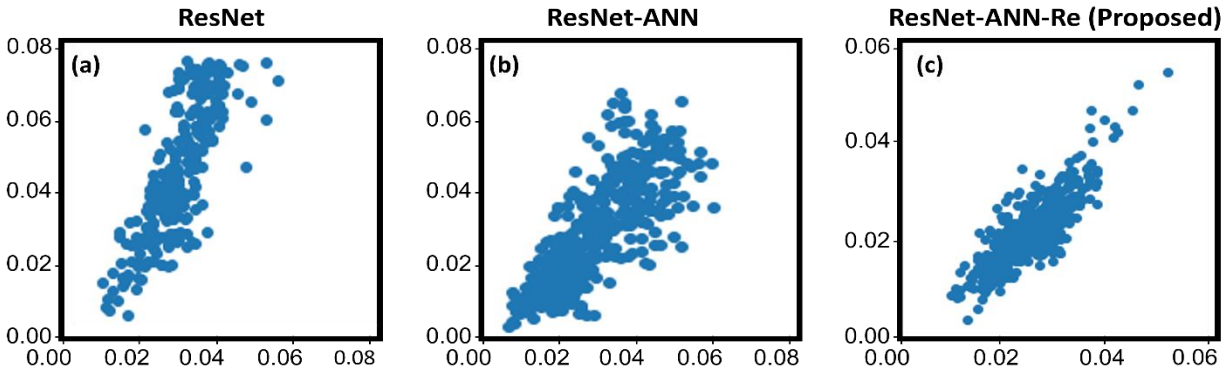

Figure 4-7: The correlation between simulated stress (horizontal axis) and predicted stress (vertical axis) by three models: a) ResNet; b) ResNet-ANN; c) ResNet-ANN-Re.

4.5 Conclusions and future work

The correlation among process parameters, process signatures, and product qualities in the AM process must be established to achieve rapid quality assurance of the metal AM system. This work develops a deep learning-based surrogate model to predict residual stress based on the process parameters and thermal history with reheating effects during the LPBF process. The results demonstrate the effectiveness of the proposed research method in achieving an improved correlation and reduced error for multi-layer residual stress prediction. The main benefit of our proposed approach is the improvement of mechanical response prediction by correlating process parameters and reheating effects of thermal cycles in the surrogate modeling. Future work of this research involves improved algorithm performance focusing on spatial-temporal features. The generalization capability would be extended to other product qualities and geometry designs.

For future work, there are few potential future works in which the algorithm performance and generalization capability can be improved. First, an exploration of including all samples from each

pattern to predict the unseen region of either pattern is expected. Second, exploring other neural network architecture that deals with spatiotemporal information to extract useful features from the time-series thermal history data is planned. Third, a potential solution is to generate a synthetic thermal history sample from simulation data using a generative adversarial network (GAN).

5. Optimal process parameter recommendation for the inverse design of product qualities

This chapter describes a sequential learning-based inverse design approach that can be used to optimize optimal process parameters to achieve desired mechanical responses achieved in AM processes. The parameter design space is crucial as AM processes have many parameters that lead to a high dimensional and complex optimal parameter design space, requiring further attention in parameter optimization. In the existing literature, neural network (NN)-based surrogate modeling has gained popularity in predicting linkages between process parameters, process signatures, and printed parts qualities. However, these neural networks are deterministic and lack quantifying predictive uncertainty, which may lead to overfitting issues. Hence, we propose a deep ensemble that employs predictive uncertainty to contribute to the inverse design of optimal parameter values for AM processes. This work will utilize a high-fidelity AM simulation dataset as training and testing data to guide deep-ensemble-based neural networks for predicting and recommending the optimal process parameter sets given mechanical response requirements. We integrate an active learning algorithm for a deep ensemble with predictive uncertainty. The case studies are based on the curated simulation dataset of the powder bed fusion AM process. The numerical study demonstrates that the proposed approach can effectively improve the performance of predictor and recommender by incorporating predictive uncertainty with fewer samples.

5.1 Introduction

AM is a promising technology that enables the fabrication of complex, graded material compositions and customized parts and devices. To take advantage of these capabilities, it is critical to explore optimal regions of process parameter design spaces given desired regions of

quality performance spaces [134]. Research utilizing physics-based simulations of AM processes to predict material properties and defects is common. In contrast, the data-driven surrogate modeling approach in this research effort is intended to replace computationally intensive and time-consuming issues inherent in physics-based simulations. However, the forward prediction model only helps answer "what-if" questions to predict parts' quality based on different combinations of process parameters. The industry is also interested in the inverse of this feed-forward prediction problem, i.e., determining the optimal combination of inputs/process parameters given a desired output/parts' quality. Such inverse problems can be formulated as optimization problems. Mohamed *et. al.* [135] reviewed extensive studies of approaches to such problems, including full factorial designs, Taguchi methods, response surface methods, genetic algorithms, machine learning, and experimental field approaches for correlating process parameters with quality results.

In the parameter optimization of AM process, 3D computer simulations are often applied to understand the relationship between processing parameters and the thermal behavior of the printed parts [46-48]. However, these computer simulations are associated with higher costs for computational execution because of complex physical models accounting for thermomechanical behaviors during printing processes. In addition, the experimental approach to exploring the design space of process parameters is tedious because there are many process parameters [136, 137] that can influence the process dynamics and the final quality of the printed part. Thus, research opportunities lie in the inverse design of parameters optimization, which is critical for achieving the desired quality of printed parts with quicker and more reliable performance.

This chapter proposes a deep ensemble with active learning (DEAL) framework to address research gaps identified in the literature. Uncertainties are inevitably present in various stages of

AM processes. These uncertainties could be identified from the experimental approach, simulation modeling, and surrogate modeling [73, 74]. In this work, we identify uncertainty sources to focus on surrogate modeling. Firstly, the proposed deep ensemble is used to incorporate prediction uncertainty into surrogate modeling, which is lacking in existing neural network architectures. Several approaches have been developed to consider and quantify prediction uncertainty in neural network applications. Most previous research efforts in this area have adopted a Bayesian architecture incorporating a prior distribution of weights in an NN and a posterior distribution of parameters to quantify predictive uncertainty. In practice, a Bayesian NN is difficult to implement with the "correct" distribution of priors and is computationally slower to train than a neural network. Thus, there is a need to develop a neural network with predictive uncertainty estimation capability that can be adapted straightforwardly to the current neural network architecture. Lakshminarayanan *et al.* [138] demonstrated the success of a simple yet scalable neural network considering predictive uncertainty, called a deep ensemble of neural networks. Their work demonstrated the proper scoring rule of negative log-likelihood as a training criterion and the implementation of an ensemble of NNs to showcase the improved predictive performance with uncertainty quantification that compared well with Bayesian NNs.

Secondly, the active learning approach is integrated into the DEAL framework to improve predictive modeling for metal AM processes with an adaptive training data sampling technique. The goal of active learning is to achieve more with less. Our framework uses active learning to achieve better predictive performance and inverse process parameter design with fewer training samples. For instance, the process parameter design space in AM manufacturing is easy to define using classic sampling techniques. However, its corresponding output responses are typically tedious, expensive, and time-consuming to acquire using computer simulations or experimental

approaches. These challenges motivated us to implement an active learning algorithm with a deep-ensemble model. We propose to utilize predictive uncertainty information to maximize the information in the data training pipeline to reduce the training dataset size while achieving better performance.

We propose a deep ensemble with an active learning (DEAL) framework to achieve an inverse process parameter design with smaller sample sizes. First, we develop a deep ensemble algorithm for adapting an existing neural network to consider predictive uncertainty. We use negative log-likelihood as the scoring rule of training criteria to yield the prediction's mean and variance. Then, we implement an ensemble of neural networks to correlate process parameters and mechanical responses for inverse process parameter design. We integrate a variance-based active learning algorithm into the deep ensemble to improve the predictive modeling and process parameter design recommendation with fewer samples. The well-trained deep-ensemble network is then utilized to optimize optimal process parameters using grid-based sampling of a process parameter design space. To the best of our knowledge, this is the first application of a deep-ensemble method with an active learning framework in the context of optimal process parameter recommendation for the inverse design of mechanical responses of AM parts.

The remainder of this chapter is organized as follows: Section 5.2 describes the theoretical background of neural networks and active learning. Section 5.3 presents the proposed DEAL framework for inverse process parameter design, including deep-ensemble and active learning algorithms. Section 5.4 presents case studies of AM application, including a background introduction of mechanical response prediction for metal AM processes and DEAL framework evaluation. Lastly, Section 5.5 summarizes the conclusions of this chapter and suggests future work.

5.2 Theoretical background

5.2.1 Neural networks

Data-driven models such as neural networks are used in a wide range of applications, such as computer vision, natural language processing, and autonomous driving. Neural networks have also emerged among AM applications for their cost-effectiveness and efficient use of computational power. The emergence of neural network applications for predicting linkages between process parameters and properties has been reviewed thoroughly in the literature [112, 139]. Neural networks are categorized as supervised machine learning in which the dataset that they learn has input features and corresponding labels. They are popular and appropriate for AM processes because there are well-defined inputs and outputs.

Determining optimal process parameters is highly desirable to achieve rapid quality assurance for AM processes. Predictive models are needed to describe relationships among process parameters, process signatures, and printed parts' qualities. However, PSQ relationships are often highly nonlinear since the process parameter design space of an AM process is typically high-dimensional and complex. Given their unique nonlinear characteristics, NN algorithms have been demonstrated to perform well in identifying PSQ relationships in AM applications. For instance, Shen *et al.* developed a two-layer neural network structure to correlate process parameters (laser power, scan speed, scan spacing, and layer thickness) with density prediction for selective laser sintering [140]. Caiazzo *et al.* [141] proposed neural network-based machine learning for correlating process parameters and printed trace geometry with good prediction performance. Zhang *et al.* [142] demonstrated the use of recurrent NN in a fused deposition modeling (FDM) process to predict the tensile strength of printed products. However, these neural networks are

deterministic and are unable to quantify predictive uncertainty. Existing neural networks are also vulnerable to adversarial examples and prone to overfitting issues [72, 143].

Uncertainty quantification is critical for designing robust models that consider various sources of uncertainty underlying the AM processes in terms of material properties, process parameters, and property measurement [74]. In surrogate modeling, it is vital to consider model uncertainty, particularly predictive uncertainty. Therefore, uncertainty estimation is necessary for neural network-based AM applications to understand their predictive model performance. A common approach to quantifying predictive uncertainty is to utilize Bayesian neural networks [144], which are difficult to set up in practice and computationally intensive to run. These disadvantages of Bayesian neural networks motivate research in adapting NNs with uncertainty quantification. Lakshminarayanan *et al.* [138] demonstrated a simpler yet scalable method called a deep neural network ensemble with predictive uncertainty consideration. Their work demonstrated the usage of negative log-likelihood as a training loss and ensemble training tool for neural networks to showcase improved uncertainty-aware predictive performance. This deep-ensemble technique has demonstrated superior performance with classical classification and regression datasets and compares well in performance with Bayesian networks. Our review of the literature discloses that little research has been done on the use of surrogate modeling for AM applications using neural networks with uncertainty. This research gap motivates our work to explore and contribute to this field by demonstrating the effectiveness of neural networks with uncertainty-aware predictions in AM applications.

5.2.2 Active learning

Active learning (AL) is iterative supervised learning that maximizes information acquisition and improves model performance with fewer training samples [145]. Active learning

for regression tasks can be thought of as a learner starting with many unknown output responses and only a small amount of input data. A learner's goal is to establish a mapping function based on limited input data. Then, the learner selects the subsequent instances from the unlabeled dataset. The instance query strategy may vary depending on the nature of the application. In the literature, many proposed active learning query strategies have been adapted to different applications. For instance, the subsequent sample can be selected based on the most uncertainty in predicting the output. As a result of the new query instance, the prediction performance improves because the least certain instances might contribute more toward it. The domain expert or oracle usually labels the query instances in this process. After obtaining the query instance's response, the instance and its output are added to the initial training set. The mapping function is then updated using a revised dataset. This process repeats until the preset stopping criteria are met or the process runs out of query budget. Hence, the AL algorithm benefits highly complex processes with constraints on the budget and computational time, especially for additive manufacturing applications [139].

Examples of AL algorithm integration into AM applications are limited in the literature. Few studies have utilized active learning in manufacturing systems, such as composite fuselage applications and additive manufacturing applications [146, 147]. For instance, Yue *et al.* [145] demonstrated a Gaussian process that considers uncertainty with a variance-based weighted active learning and a D-optimal weighted active learning algorithm. Their work showed that proposed active learning strategies could improve the predictive modeling for composite fuselage applications. Van Houtum and Vlasea [146] integrated an active learning algorithm to classify melt-pool quality conditions for the DED process via an adaptive weighted uncertainty sampling strategy. Their proposed active learning method reduces the data necessary for achieving desired DED quality conditions with a low-cost computational advantage. Dasari *et al.* [147] showcased

the application of active learning in reducing the number of data samples required to develop classification models for in situ process monitoring in AM. Their work utilized clustering and committee-based sampling techniques to decrease the amount of data labeling required by the AM processes for condition classification.

The literature shows that active learning can be used for performance prediction with fewer samples. However, in previous studies [146] and [147], active learning has been used mainly for classification tasks. Therefore, we identify this as a research gap to be filled by integrating active learning into a deep-ensemble framework for effective training data selection for neural networks.

5.3 Deep ensemble with active learning (DEAL) framework

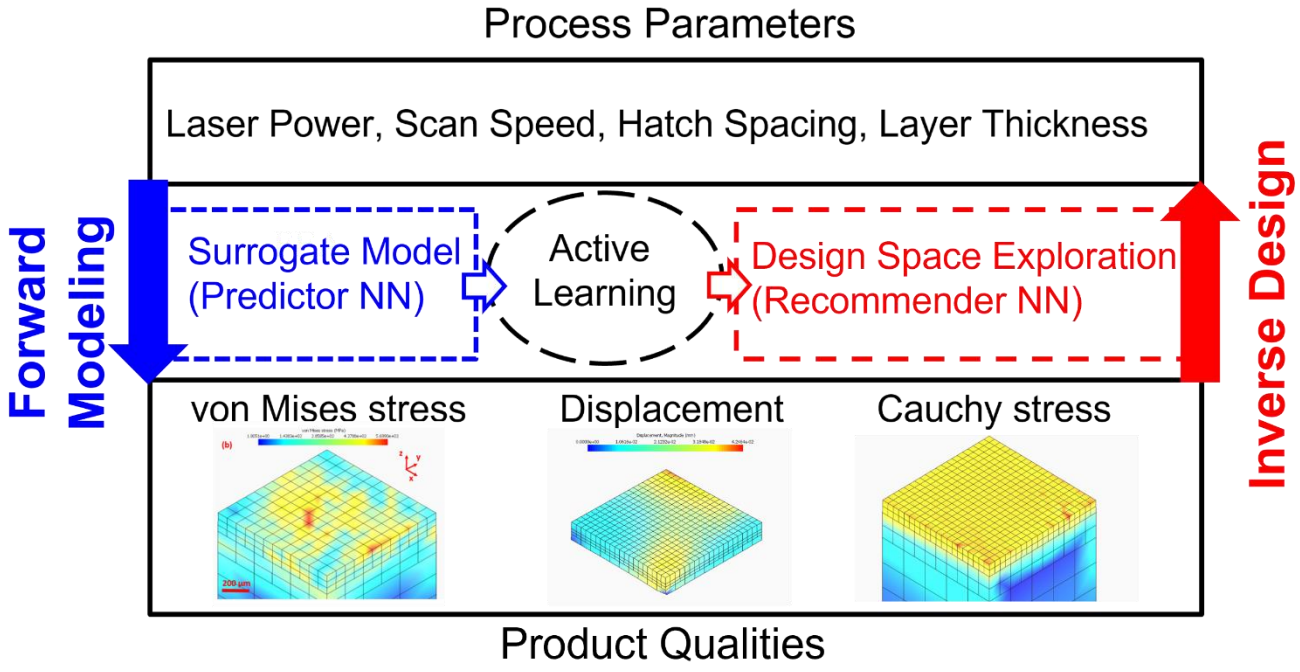

Figure 5-1: The DEAL framework flow involves forward modeling and inverse design from process parameters to product qualities and vice versa. The DEAL framework utilizes a predictor neural network as a surrogate model, a recommender neural network for design space exploration, and active learning algorithms for effective data sampling.

The proposed deep ensemble with active learning (DEAL) framework aims to achieve optimal process parameter recommendation for the inverse design of mechanical responses of AM parts with predictive-aware uncertainty and fewer training samples. Hence, the DEAL framework comprises two major components: deep ensembles (DE) and active learning (AL). The research framework architecture using DEAL, illustrated in Figure 5-1, consists of two deep ensembles, a predictor and a recommender, and an active learning algorithm as a learner.

5.3.1 Predictor neural network

A deep ensemble is an ensemble of neural networks that uses a proper scoring rule as the training criterion to achieve predictive uncertainty [138]. The deep-ensemble algorithm can be formulated as follows:

$$\mathrm{S} = \{x_n, y_n\}_{\mathrm{n}=1}^{N} \tag{16}$$

where S is the dataset, N is the total number of data samples, $x_n \in \mathbb{R}^D$ denotes the D-dimensional set of features of the input space, and $y_n \subset \mathbb{R}$ is the set of prediction responses in the output space. The deep-ensemble method utilizes a neural network that represents the probabilistic predictive distribution $p_\theta(\mathrm{y}|\mathrm{x})$, where θ represents the parameters of the neural network.

The two key aspects of a deep ensemble that employs predictive uncertainty are 1) using a proper scoring rule as the training requirement and 2) training an ensemble of neural networks. First, a proper scoring rule is defined as a quality measurement of predictive uncertainty that rewards better-calibrated predictions. In this deep-ensemble formulation, we minimize the negative log-likelihood loss as described as follows:

$$-\log p_\theta(y_n|x_n) = \frac{\log \sigma_\theta^2(x)}{2} + \frac{(y-\mu_\theta(x))^2}{2\sigma_\theta^2(x)} + constant \tag{17}$$

The major difference between a deep ensemble and a plain neural network is that a deep ensemble has two outputs in the final layer corresponding to the predicted mean and variance

[148]. This additional variance layer can be achieved by adding a new Gaussian layer and treating the observed value as a sample from a Gaussian distribution.

Second, we train an ensemble of independent neural networks simultaneously. Ensemble techniques are not uncommon in machine learning research, as a wide variety of methods exist to improve the performance of neural network-based applications [149-151]. We utilize random subsamples of the data at each iteration and a random initiation of the neural network parameters. As a result, the ensemble of neural networks is a uniformly weighted mixture model with combined predictions, which is written as follows:

$$p(y|x) = M^{-1} \sum_{m=1}^{M} p_{\theta_m}(y|x, \theta_m) \tag{18}$$

where M is the number of neural networks in the deep ensemble and p_{θ_m} is the probabilistic predictive distribution.

In the following case study, we designed a base neural network with three hidden layers of 128 neurons, 64 neurons, and 32 neurons, respectively. We deployed M = 5 neural networks for the deep ensemble of five base neural networks. The deep-ensemble model was trained using an Adam optimizer with a learning rate of 0.001, a batch size of 32, and 500 epochs. The model was trained using two NVIDIA GeForce RTX 2080 Ti GPUs and the TensorFlow Keras library [130]. We used a grid search cross-validation for hyperparameter tuning to determine these neural network parameters. The dataset was split between training (60%), validation (10%), and testing (30%) subsets.

5.3.2 Recommender neural network

In contrast to a previous study [138], we adapted a deep ensemble for the recommender neural network. The goal was to recommend optimal process parameters, given the inverse design of the desired mechanical responses of AM processes. Unlike the predictor neural network, the

role of the recommender neural network performs is as an inverse design model in which the weights and biases of parameters are not learnable. The learning outcomes in the recommender neural network are the process parameter variables. In our case study, the objective of the recommender neural network was to recommend the top five process parameter settings that achieve each desired mechanical response. The process parameter designs are initiated by a grid-based sampling approach, maximin Latin hypercube sampling (LHS) [152]. These process parameter designs are different from the training data sets, which are not seen or used in the training pipeline. Then, these process parameter settings are treated as the inputs of the recommender neural network. The outputs of the recommender neural network are the top five process parameter variables that meet the objective functions of multiple mechanical response prediction. The top five optimal process parameter variables from each objective function are selected and verified by a physics-based simulation oracle.

5.3.3 Active learning

In this section, we propose integrating the active learning algorithm into the deep-ensemble framework to reduce the number of training samples required to improve prediction performance and optimal process parameter recommendation. The integration flow of the active learning algorithm with the predictor and recommender neural networks is illustrated in Figure 5-2. The primary setup difference is that this DEAL framework starts with a small dataset and improves its predictive performance by adding new data samples sequentially with an effective active learning strategy.

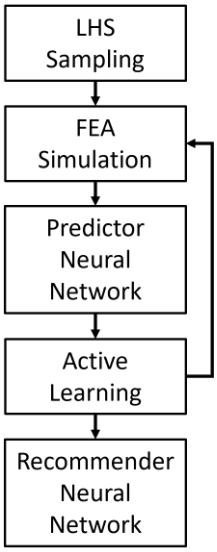

Figure 5-2: Integration flow of active learning algorithms with predictor neural network and recommender neural network.

The core of the active learning algorithm is to select the subsequent sample wisely, as this is a significant component of active learning for regression tasks. Given that subsequent samples are chosen from within the sample pool, we can define these samples as $\hbar = \{\hbar_1, \hbar_1, \ldots., \hbar_n\}$, where n denotes the size of the sample pool $\hbar$. The recommended active learning strategy can be viewed as a balanced trade-off between the exploitation and exploration of the sample pool. In this active learning approach, the maximin Latin hypercube design [152] was selected to obtain the initial samples in the sample pool. Since a deep ensemble is trained with predictive uncertainty, the output variance of its prediction can be further utilized for the active learning query strategy. Therefore, we suggest a variance-based active learning query strategy for the deep ensemble, written as follows:

$$\hbar_{new} = \arg_{\hbar \in \{\hbar_1, \hbar_1, \ldots., \hbar_n\}} \max \sum_{m=1}^{M} Var_m = M^{-1} \sum_{m} \left({\sigma^2}_{\theta_m}(x) + {\mu^2}_{\theta_m}(x) \right) - \mu_*^2(x) \qquad (19)$$

where $\hbar_{new}$ is the subsequent sample query and Var_m is the variance of the deep ensemble for the predictor neural network.

We utilized model parameters from the deep ensemble considering predictive uncertainty to evaluate the sample pool for fully implementing the variance-based active learning strategy. The deep-ensemble predictor calculates the variance of each sample query. Then, the new sample query $\hbar_{new}$ is chosen that meets the variance requirement, as described by Equation 19. The oracle used in this active learning framework is the FEM simulation that provides output responses Y($\hbar_{new}$). The deep-ensemble predictor is first trained with 20 samples that are randomized from the sample pool. This initial sample number was selected based on a rule of thumb mentioned in the literature [145] that it should be five times the number of investigated process parameters. The size of dataset S was updated and increased iteratively by adding new sample queries and their corresponding responses. A new set S was trained sequentially to update its predictive performance and uncertainty. The procedures were repeatedly updated by adding new samples to dataset S until the stopping criteria were met. The process stopped when the iteration number reached the maximum allowable number of iterations.

5.4 Case studies

To validate the effectiveness of our proposed DEAL framework, we conduct a real-world case study regarding optimal process parameter recommendations for the inverse design of desired mechanical responses of the AM process. First, we introduce the case study background regarding multiple mechanical response prediction of metal AM processes, as detailed in Section 5.4.1. We describe the performance evaluation metrics of the DEAL framework in Section 5.4.2. We discuss the results of the DEAL framework in Section 5.4.3.

5.4.1 Mechanical response prediction of metal AM simulation

The objective of this case study is to recommend optimal process parameter settings given desired mechanical responses of an AM process. We used Autodesk Netfabb Local Simulation to

generate high-fidelity data for the proposed framework. The simulator provides the flexibility to select process parameters—laser power, travel speed, layer thickness, and hatching pattern parameters—as thermal simulation model inputs, using common AM materials or customized materials in the library. As a result, for the data curation of this case study, a Ti-6Al-4V alloy material was selected for the study with four significant parameters: laser scan speed, power, hatch spacing, and layer thickness. The outputs considered in this case study were the von Mises stress, displacement, and Cauchy stress, as these mechanical responses are deemed significant variables affecting AM parts' quality. The ranges of these process parameters were chosen for an operating range described in the literature [49, 104] to create a more extensive dataset covering the typical range of metal AM processes. The chosen part design was a box 2 mm × 2 mm square and three layers in height. One thousand data samples were generated from the simulation model using the maximin Latin hypercube sampling (LHS) method [152]. The input bounds for each parameter are listed in Table 5-1.

Table 5-1: Input bounds for each process parameter in the initial data sampling approach.

Process Parameters	Unit	Low Range	High Range
Laser speed	mm/s	150	1150
Laser power	W	50	350
Layer thickness	mm	0.02	0.12
Hatch spacing	mm	0.08	0.18

5.4.2 DEAL framework performance evaluation

To demonstrate the performance of the proposed DEAL framework, we introduced the following evaluation criteria for each component of the DEAL framework, including the predictor neural network and recommender neural networks. In addition, we evaluated the data sample efficiency of the deep-ensemble case with an active learning algorithm.

For the performance comparison of the predictor and recommender neural networks, seven widely used regression-based machine learning algorithms—a Bayesian neural network (BNN), XGB regressor, random forest regressor, KNN regressor, GP regressor, support vector regressor, and standard neural network—were selected as the benchmarks for the predictor neural network. A Bayesian neural network is a neural network with a probabilistic structure that incorporates distributions statistics. However, the BNN used is difficult to tune. The settings used for the BNN were two layers with dense variational structures, trained with 1000 epochs. The standard NN is a common MLP architecture for AM process parameter prediction. The standard NN settings, like those of our proposed DE method, consisted of three MLP layers.

The regression algorithms were trained to predict multiple mechanical responses for the predictor neural network evaluation criterion. The prediction performance of predictor neural networks was evaluated using the common regression metrics, namely, the root mean square error (RMSE) and correlation coefficient (CC) between the predicted and simulated output responses for the predictor neural network. The higher the CC is, the better the model predicts the trend. Ten replications were repeated for the predictor neural networks.

The goal of the optimal process parameter recommendation in this AM case study was to minimize certain mechanical responses, including the maximum von Mises stress, maximum displacement magnitude, and maximum Cauchy stress magnitude. For the recommender neural network evaluation criterion, the trained regression algorithms were used to recommend the top five parameter sets from the unseen testing pool of 300 process parameter settings. Given each objective function of the mechanical responses, the top five parameter sets that minimized each mechanical response were selected and compared with the actual top five parameter sets from the testing pool. The recommendation performance of the recommender neural network was measured

by three evaluation metrics: recommendation accuracy, RMSE, and relative error (RE) between the predicted and actual top five process parameter settings for the recommender neural network. Ten replications were repeated for the recommender neural networks.

The goal of the active learning integration with the deep ensemble is to demonstrate the effectiveness of the active learning algorithm in reducing the number of data samples required by the neural networks to achieve performance similar to that achievable using the entire data sample set. For the evaluation criterion for the active learner, we applied our proposed deep ensemble for the predictor and recommender neural networks to verify its mechanical property prediction ability and assess its performance in recommending the top five parameter settings. The variance-based active learning approach and three widely used regression-based methods—random, Upper Confidence Bound (UCB), and maximin distance—were compared to assess the effectiveness of the DEAL framework. The stopping criteria for active learning were set by limiting the number of iterations to 130 queries. Ten replications were repeated for the active learning algorithms.

5.4.3 DEAL framework validation results

The validation results of the DEAL framework are demonstrated to showcase the effectiveness of the predictor neural network in Section 5.4.3.1, the recommender neural network in Section 5.4.3.2, and deep-ensemble networks with active learning in Section 5.4.3.3.

5.4.3.1 Predictor Neural Network

The evaluation criteria for the predictor neural network were introduced in Section 5.4.2. The average of CC and RMSE for each mechanical property among the proposed and benchmark methods are summarized in Table 5-2. The methods were applied based on the entire training sample with ten replications. It is evident that the proposed deep-ensemble algorithm outperforms the benchmark methods in terms of all evaluation metrics. The results demonstrate that the

performance of a standard neural network can be further improved by incorporating prediction uncertainty, an appropriate training loss criterion, and the ensemble technique.

Table 5-2: Performance comparison between the deep-ensemble method and benchmark algorithms for predictor neural network.

	von Mises stress		**Displacement**		**Cauchy stress**		**Average**	
Method	**CC**	**RMSE**	**CC**	**RMSE**	**CC**	**RMSE**	**CC**	**RMSE**
BNN	0.750	0.101	0.716	0.143	0.658	0.179	0.708	0.141
XGB	0.856	0.079	0.866	0.077	0.722	0.094	0.814	0.083
Random Forest	0.904	0.064	0.853	0.080	0.773	0.085	0.825	0.080
kNN	0.891	0.068	0.865	0.077	0.795	0.080	0.851	0.075
GP	0.956	0.043	0.919	0.059	0.829	0.073	0.901	0.060
Support Vector	0.887	0.070	0.784	0.082	0.856	0.073	0.856	0.073
Standard NN	0.960	0.041	0.928	0.056	0.863	0.066	0.917	0.055
Deep Ensemble	**0.984**	**0.025**	**0.930**	**0.054**	**0.907**	**0.062**	**0.940**	**0.047**

5.4.3.2 Recommender Neural Network

For the recommender neural network, the performance comparison between the deep ensemble and other benchmark algorithms is summarized in Table 5-3. The top five optimal process parameters for each mechanical property (von Mises stress, displacement, and Cauchy stress) are identified and compared with the recommended process parameter predicted by the recommender neural network under the listed methods. The recommender neural network aims to correctly identify the top five optimal process parameters with small RMSE and RE. The results show that the deep-ensemble model outperforms all other benchmark methods. It is evident that the deep-ensemble-based recommender neural network can provide an effective recommendation for the top five optimal process parameters of each objective function of desired mechanical responses. One observation from the performance is that the ensemble technique provides a better recommendation by aggregating the decisions from an ensemble of independent neural networks by utilizing the maximum information of predictive uncertainty, which is lacking in the standard neural networks.

Table 5-3*:* Performance comparison between the deep-ensemble method and benchmark algorithms for the recommender neural network.

	von Mises stress			**Displacement**			**Cauchy stress**		
Method	**Accuracy**	**RMSE**	**RE**	**Accuracy**	**RMSE**	**RE**	**Accuracy**	**RMSE**	**RE**
BNN	0.75	0.092	0.097	0.68	0.194	0.143	0.54	0.092	0.243
XGB	0.84	0.073	0.056	0.84	0.109	0.086	0.62	0.061	0.142
Random Forest	0.90	0.032	0.071	0.84	0.113	0.068	0.68	0.046	0.125
kNN	0.90	0.062	0.041	0.84	0.113	0.088	0.70	0.043	0.107
GP	0.94	0.029	0.056	0.88	0.107	0.075	0.72	0.041	0.092
Support Vector	0.88	0.081	0.059	0.80	0.142	0.092	0.74	0.037	0.082
Standard NN	0.94	0.044	0.048	0.90	0.105	0.115	0.76	0.039	0.075
Deep Ensemble	**0.98**	**0.019**	**0.037**	**0.90**	**0.064**	**0.055**	**0.80**	**0.038**	**0.069**

5.4.3.3 Deep Ensemble with Active Learning Framework

We evaluated four common active learning strategies used for regression tasks. The performance comparison for the correlation coefficients of the four active learning strategies, namely, random, maximin, Upper Confidence Bound (UCB), and variance, is summarized in Table 5-4. It is evident that active learning strategies achieve relatively good performance with only 150 data samples. Among the four active learning methods, the variance-based approach outperforms the other active learning strategies, indicating that the variance information from the deep ensemble can be utilized for effective data sampling selection. Figure 5-3 illustrates the active learning curves for the correlation coefficients of the four active learning strategies. Figure 5-3 shows that as the number of queries increases, the performance metrics improve because more informative samples are added to enhance the predictive models. Figure 5-3 also shows that the variance-based active learning algorithm outperforms the other three approaches. The deep-ensemble model with variance-based active learning strategy achieves a 0.886 average correlation coefficient with only 130 additional queries.

Table 5-4: Performance comparison of the deep-ensemble method with different active learning strategies for predictor neural network.

	von Mises stress		Displacement		Cauchy stress		Average	
Method	**CC**	**RMSE**	**CC**	**RMSE**	**CC**	**RMSE**	**CC**	**RMSE**
Random	0.917	0.060	0.901	0.068	0.754	0.088	0.859	0.073
Maximin	0.915	0.060	0.912	0.061	0.774	0.086	0.867	0.071
UCB	0.923	0.057	0.925	0.061	0.755	0.089	0.869	0.071
Variance	**0.928**	**0.055**	**0.934**	**0.052**	**0.798**	**0.084**	**0.886**	**0.067**

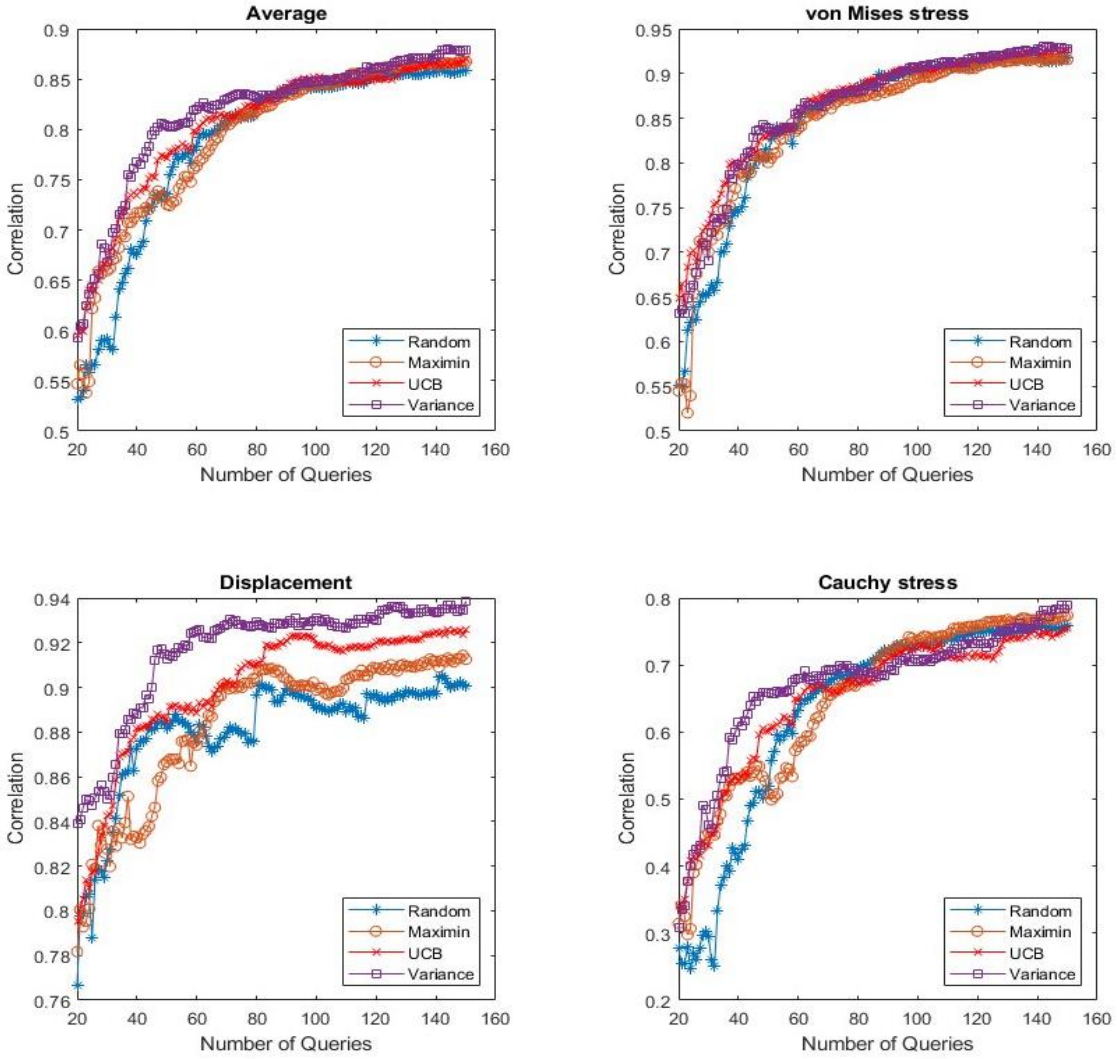

Figure 5-3: Active learning curves for the correlation coefficients of active learning strategies, namely, random, maximin, UCB, and variance.

Figure 5-4 shows that the variance-based active learning strategy outperforms the other three active learning strategies in terms of the RMSE performance metric for all mechanical

response cases. In the von Mises stress case, the variance-based active learning strategy achieves a 0.94 correlation coefficient and 0.049 RMSE within 130 sample queries. In summary, the proposed active learning-based algorithms achieve a 78.5% training data sample size reduction for the predictor neural network compared with 700 samples from the entire training data set. To further validate the performance of the recommender neural network with an active learning framework, Table 5-5 compares the performance of the deep-ensemble method with four methods: random, maximin, UCB, and variance. Table 5-5 shows that recommender neural networks with smaller training samples can achieve comparable performance across performance metrics by utilizing active learning strategies. Among these active learning strategies, the variance-based sampling approach performs the best in that it achieves the highest accuracy, lowest RMSE, and lowest RE in all cases of inverse design of mechanical responses.

Table 5-5: Performance comparison of the deep-ensemble method with different active learning strategies for neural recommender network

	von Mises stress			**Displacement**			**Cauchy stress**		
Method	**Accuracy**	**RMSE**	**RE**	**Accuracy**	**RMSE**	**RE**	**Accuracy**	**RMSE**	**RE**
Random	0.88	0.061	0.077	0.82	0.084	0.069	0.68	0.107	0.085
Maximin	0.88	0.058	0.057	0.84	0.076	0.073	0.70	0.084	0.081
UCB	0.90	0.051	0.049	0.86	0.076	0.069	0.68	0.094	0.075
Variance	**0.94**	**0.049**	**0.047**	**0.88**	**0.069**	**0.063**	**0.74**	**0.077**	**0.076**

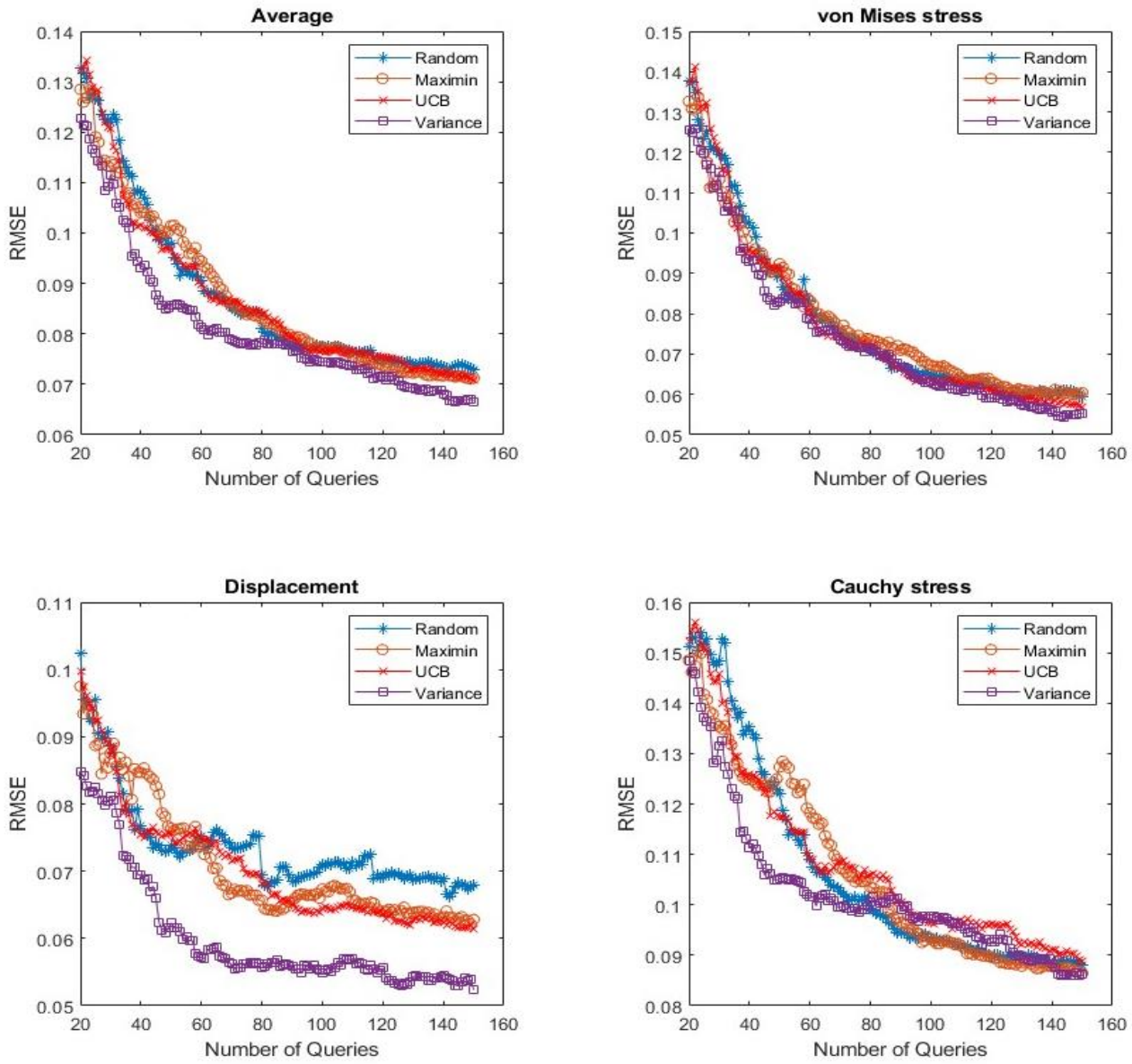

Figure 5-4: Active learning curves for the correlation coefficients of active learning strategies, namely, random, maximin, UCB, and variance.

5.5 Conclusions and future work

This research work developed deep-ensemble neural networks with active learning (DEAL) framework to optimize optimal process parameters for the inverse design of mechanical responses in the metal AM process. Specifically, the proposed DEAL framework allows computationally expensive physical-based simulation models to be replaced by data-driven surrogate models that can determine optimal parameters to achieve desired quality properties. This

work identifies the existing research gaps: 1) predictive uncertainty in existing neural network-based AM applications, 2) inverse design of determining optimal parameter values is crucial for AM applications, and 3) information on data training sampling for existing neural networks is lacking. The proposed research framework fills these gaps by providing an alternative yet rapid inverse design solution in place of time-consuming simulation or experimentation data for achieving a smart quality assurance system for AM processes.

For the DE-based predictor neural network, a deep ensemble considering predictive uncertainty was proposed to improve the predictive performance of multiple mechanical responses of AM process. The results from the deep-ensemble predictor achieved the best among seven other benchmark methods. The evaluation metrics for the DE-based recommender neural network, including recommendation accuracy, RMSE, and RE, showed that the proposed DEAL framework achieved the best performance for optimal process parameter recommendation compared with the benchmark methods. An active-learning-based DE-based neural network was developed to implement effective data sample reduction. The case study with active learning integration showed that the integrated active learning framework is very effective for making optimal process parameter recommendations with fewer samples, as demonstrated by the 78.5% data sample size reduction.

6. Conclusion and future research

This dissertation presents a data-driven PSQ framework for implementing and ensuring quality assurance in AM processes. Three data-driven approaches—DoE, forward prediction modeling, and inverse design—are integrated to identify the correlations among process parameters, process signatures, and product qualities. Two major AM processes (bioprinting and metal AM) were used to validate the proposed frameworks with three different materials (PLA polymer, Pluronic F127 hydrogel, and Ti-6Al-4V alloy). The challenges associated with the aforementioned AM processes, such as the labor-intensive trial-and-error approach, nonlinear process dynamics between thermal and mechanical responses, and high-dimensional process parameter design space, are addressed successfully by the proposed approaches, which are more data-driven, adaptable, and applicable to other domains of manufacturing systems.

The primary goal of this dissertation research was to develop a smart quality assurance system using a data-driven-based PSQ framework using DoE, forward prediction modeling, and inverse design in AM processes. The main contributions of this research effort are identified as follows:

1. **Learning the relationships between process parameters, process signature, and parts quality during bioprinting processes:** Novel bioprinting in a multimaterial scaffold application is demonstrated to learn the relationships among process parameters and corresponding parts' quality using an in-process sensing platform that is integrated with statistical DoE techniques to implement process mapping and optimization for bioprinting (Chapter 3).
2. **Developing a PSQ framework for the forward prediction problem in estimating printed parts' quality:** A novel deep-learning-based surrogate model was developed

using high-fidelity physics-based simulated AM data to predict the residual stress of AM printed parts (Chapter 4).

3. **Recommending optimal process parameters achieving desired printed parts quality of AM processes:** A novel active learning-based deep-ensemble framework is developed to recommend optimal process parameters for the inverse design of the desired mechanical responses requirement with fewer data samples. (Chapter 5).

Specifically, the PSQ-oriented smart quality assurance framework was developed and implemented using statistical analysis and advanced surrogate modeling with high-dimensional process data acquired from in-process sensing platforms and physics-based computer simulation models. Three proposed framework holds promise for use in rapid quality assurance systems for two major additive manufacturing processes: extrusion-based bioprinting and laser-based metal AM process.

The proposed smart quality assurance system framework was initiated with clear research objectives and tasks. In the future, the following two research areas will be of great interest in extending the work described in this dissertation.

1. PSQ framework extension to multi-scale modeling and multi-physics of AM applications:

   The first area to explore in extending the data-driven PSQ framework is the process–structure–property–performance (PSPP) linkage, which involves multi-scale modeling and multi-physics phenomena. The data-driven framework proposed in this dissertation can be used to develop a smart quality assurance system by identifying the linkage between scales and physical phenomena.

2. Uncertainty-awareness-based surrogate modeling for AM applications: The second area of future work is extending the uncertainty quantification of surrogate modeling by

considering both predictive uncertainty and uncertainties in process parameters and material properties. The deep-ensemble method with predictive uncertainty described in this dissertation can be utilized as an initial framework to integrate more sources of uncertainty identified throughout AM processes, including model uncertainty, input/output uncertainty, and experimental uncertainty.

References

[1] Z. Y. Chua, I. H. Ahn, and S. K. Moon, "Process monitoring and inspection systems in metal additive manufacturing: Status and applications," *International Journal of Precision Engineering and Manufacturing-Green Technology*, vol. 4, no. 2, pp. 235-245, 2017.

[2] G. Tapia and A. Elwany, "A review on process monitoring and control in metal-based additive manufacturing," *Journal of Manufacturing Science and Engineering,* vol. 136, no. 6, 2014.

[3] M. Mani, B. M. Lane, M. A. Donmez, S. C. Feng, and S. P. Moylan, "A review on measurement science needs for real-time control of additive manufacturing metal powder bed fusion processes," *International Journal of Production Research,* vol. 55, no. 5, pp. 1400-1418, 2017.

[4] M. Mani, S. Feng, L. Brandon, A. Donmez, S. Moylan, and R. Fesperman, *Measurement science needs for real-time control of additive manufacturing powder-bed fusion processes*. CRC Press, 2017.

[5] M. L. Mather, S. P. Morgan, and J. A. Crowe, "Meeting the needs of monitoring in tissue engineering," 2007.

[6] A. Gleadall, D. Visscher, J. Yang, D. Thomas, and J. Segal, "Review of additive manufactured tissue engineering scaffolds: relationship between geometry and performance," *Burns & trauma,* vol. 6, 2018.

[7] K. Kang, L. Hockaday, and J. Butcher, "Quantitative optimization of solid freeform deposition of aqueous hydrogels," *Biofabrication,* vol. 5, no. 3, p. 035001, 2013.

[8] S. Knowlton, S. Anand, T. Shah, and S. Tasoglu, "Bioprinting for neural tissue engineering," *Trends in neurosciences,* vol. 41, no. 1, pp. 31-46, 2018.

[9] I. Matai, G. Kaur, A. Seyedsalehi, A. McClinton, and C. T. Laurencin, "Progress in 3D bioprinting technology for tissue/organ regenerative engineering," *Biomaterials,* vol. 226, p. 119536, 2020.

[10] S. Tian, H. Zhao, and N. Lewinski, "Key parameters and applications of extrusion-based bioprinting," *Bioprinting,* p. e00156, 2021.

[11] P. Moshayedi *et al.*, "Systematic optimization of an engineered hydrogel allows for selective control of human neural stem cell survival and differentiation after transplantation in the stroke brain," *Biomaterials,* vol. 105, pp. 145-155, 2016.

[12] J. Lam, S. T. Carmichael, W. E. Lowry, and T. Segura, "Hydrogel design of experiments methodology to optimize hydrogel for iPSC-NPC culture," *Advanced healthcare materials,* vol. 4, no. 4, pp. 534-539, 2015.

[13] L. R. Nih *et al.*, "Engineered HA hydrogel for stem cell transplantation in the brain: Biocompatibility data using a design of experiment approach," *Data in brief,* vol. 10, pp. 202-209, 2017.

[14] L. A. Smith Callahan, "Combinatorial method/high throughput strategies for hydrogel optimization in tissue engineering applications," *Gels,* vol. 2, no. 2, p. 18, 2016.

[15] T. Huber, H. Najaf Zadeh, S. Feast, T. Roughan, and C. Fee, "3D Printing of Gelled and Cross-Linked Cellulose Solutions, an Exploration of Printing Parameters and Gel Behaviour," *Bioengineering,* vol. 7, no. 2, p. 30, 2020.

[16] E. Carlier *et al.*, "Investigation of the parameters used in fused deposition modeling of poly (lactic acid) to optimize 3D printing sessions," *International journal of pharmaceutics,* vol. 565, pp. 367-377, 2019.

[17] A. J. Guerra *et al.*, "Optimization of photocrosslinkable resin components and 3D printing process parameters," *Acta biomaterialia,* vol. 97, pp. 154-161, 2019.

[18] M. V. Gonzalez Corrales, "Optimization of bio-printing process using Design of Experiments (DOE) and Taguchi Method," 2013.

[19] J. E. Trachtenberg *et al.*, "Extrusion-based 3D printing of poly (propylene fumarate) in a full-factorial design," *ACS Biomaterials Science & Engineering,* vol. 2, no. 10, pp. 1771-1780, 2016.

[20] A. A. Armstrong, A. G. Alleyne, and A. J. W. Johnson, "1D and 2D error assessment and correction for extrusion-based bioprinting using process sensing and control strategies," *Biofabrication,* vol. 12, no. 4, p. 045023, 2020.

[21] L. Wang, M.-e. Xu, L. Luo, Y. Zhou, and P. Si, "Iterative feedback bio-printing-derived cell-laden hydrogel scaffolds with optimal geometrical fidelity and cellular controllability," *Scientific reports,* vol. 8, no. 1, pp. 1-13, 2018.

[22] W.-I. Cho, S.-J. Na, C. Thomy, and F. Vollertsen, "Numerical simulation of molten pool dynamics in high power disk laser welding," *Journal of Materials Processing Technology,* vol. 212, no. 1, pp. 262-275, 2012.

[23] L. E. Murr *et al.*, "Metal fabrication by additive manufacturing using laser and electron beam melting technologies," *Journal of Materials Science & Technology,* vol. 28, no. 1, pp. 1-14, 2012.

[24] P. Promoppatum *et al.*, "Numerical modeling and experimental validation of thermal history and microstructure for additive manufacturing of an Inconel 718 product," *Progress in Additive Manufacturing,* vol. 3, no. 1, pp. 15-32, 2018.

[25] C. Körner, E. Attar, and P. Heinl, "Mesoscopic simulation of selective beam melting processes," *Journal of Materials Processing Technology,* vol. 211, no. 6, pp. 978-987, 2011.

[26] A. Foroozmehr, M. Badrossamay, E. Foroozmehr, and S. i. Golabi, "Finite element simulation of selective laser melting process considering optical penetration depth of laser in powder bed," *Materials & Design,* vol. 89, pp. 255-263, 2016.

[27] B. Liu, G. Fang, L. Lei, and W. Liu, "A new ray tracing heat source model for mesoscale CFD simulation of selective laser melting (SLM)," *Applied Mathematical Modelling,* vol. 79, pp. 506-520, 2020.

[28] B. Richter *et al.*, "High-speed X-ray investigation of melt dynamics during continuous-wave laser remelting of selective laser melted Co-Cr alloy," *CIRP Annals,* vol. 68, no. 1, pp. 229-232, 2019.

[29] C. L. A. Leung, S. Marussi, R. C. Atwood, M. Towrie, P. J. Withers, and P. D. Lee, "In situ X-ray imaging of defect and molten pool dynamics in laser additive manufacturing," *Nature communications,* vol. 9, no. 1, pp. 1-9, 2018.

[30] P. Foteinopoulos, A. Papacharalampopoulos, and P. Stavropoulos, "On thermal modeling of Additive Manufacturing processes," *CIRP Journal of Manufacturing Science and Technology,* vol. 20, pp. 66-83, 2018.

[31] J. Romano, L. Ladani, and M. Sadowski, "Thermal modeling of laser based additive manufacturing processes within common materials," *Procedia Manufacturing,* vol. 1, pp. 238-250, 2015.

[32] P. Peyre, P. Aubry, R. Fabbro, R. Neveu, and A. Longuet, "Analytical and numerical modelling of the direct metal deposition laser process," *Journal of Physics D: Applied Physics,* vol. 41, no. 2, p. 025403, 2008.

[33] E. R. Denlinger, M. Gouge, J. Irwin, and P. Michaleris, "Thermomechanical model development and in situ experimental validation of the Laser Powder-Bed Fusion process," *Additive Manufacturing,* vol. 16, pp. 73-80, 2017.

[34] T. Gatsos, K. A. Elsayed, Y. Zhai, and D. A. Lados, "Review on computational modeling of process–microstructure–property relationships in metal additive manufacturing," *JOM,* vol. 72, no. 1, pp. 403-419, 2020.

[35] S. A. Khairallah, A. T. Anderson, A. Rubenchik, and W. E. King, "Laser powder-bed fusion additive manufacturing: Physics of complex melt flow and formation mechanisms of pores, spatter, and denudation zones," *Acta Materialia,* vol. 108, pp. 36-45, 2016.

[36] T. Mukherjee, J. Zuback, W. Zhang, and T. DebRoy, "Residual stresses and distortion in additively manufactured compositionally graded and dissimilar joints," *Computational Materials Science,* vol. 143, pp. 325-337, 2018.

[37] L. Wang, X. Jiang, Y. Zhu, X. Zhu, J. Sun, and B. Yan, "An approach to predict the residual stress and distortion during the selective laser melting of AlSi10Mg parts," *The International Journal of Advanced Manufacturing Technology,* vol. 97, no. 9-12, pp. 3535-3546, 2018.

[38] Y. Yang, M. Jamshidinia, P. Boulware, and S. Kelly, "Prediction of microstructure, residual stress, and deformation in laser powder bed fusion process," *Computational Mechanics,* vol. 61, no. 5, pp. 599-615, 2018.

[39] O. Fergani, F. Berto, T. Welo, and S. Liang, "Analytical modelling of residual stress in additive manufacturing," *Fatigue & Fracture of Engineering Materials & Structures,* vol. 40, no. 6, pp. 971-978, 2017.

[40] D. Pal, N. Patil, K. Zeng, and B. Stucker, "An integrated approach to additive manufacturing simulations using physics based, coupled multiscale process modeling," *Journal of Manufacturing Science and Engineering,* vol. 136, no. 6, 2014.

[41] G. Campoli, M. Borleffs, S. A. Yavari, R. Wauthle, H. Weinans, and A. A. Zadpoor, "Mechanical properties of open-cell metallic biomaterials manufactured using additive manufacturing," *Materials & Design,* vol. 49, pp. 957-965, 2013.

[42] B. J. Hayes *et al.*, "Predicting tensile properties of Ti-6Al-4V produced via directed energy deposition," *Acta Materialia,* vol. 133, pp. 120-133, 2017.

[43] G. Tapia, A. H. Elwany, and H. Sang, "Prediction of porosity in metal-based additive manufacturing using spatial Gaussian process models," *Additive Manufacturing,* vol. 12, pp. 282-290, 2016.

[44] J. Francis and L. Bian, "Deep learning for distortion prediction in laser-based additive manufacturing using big data," *Manufacturing Letters,* vol. 20, pp. 10-14, 2019.

[45] M. Mozaffar *et al.*, "Data-driven prediction of the high-dimensional thermal history in directed energy deposition processes via recurrent neural networks," *Manufacturing letters,* vol. 18, pp. 35-39, 2018.

[46] S. A. Khairallah and A. Anderson, "Mesoscopic simulation model of selective laser melting of stainless steel powder," *Journal of Materials Processing Technology,* vol. 214, no. 11, pp. 2627-2636, 2014.

[47] N. Hodge, R. Ferencz, and J. Solberg, "Implementation of a thermomechanical model for the simulation of selective laser melting," *Computational Mechanics,* vol. 54, no. 1, pp. 33-51, 2014.

[48] A. Gusarov, I. Yadroitsev, P. Bertrand, and I. Smurov, "Model of radiation and heat transfer in laser-powder interaction zone at selective laser melting," *Journal of heat transfer,* vol. 131, no. 7, 2009.

[49] E. R. Denlinger and P. Michaleris, "Mitigation of distortion in large additive manufacturing parts," *Proceedings of the Institution of Mechanical Engineers, Part B: Journal of Engineering Manufacture,* vol. 231, no. 6, pp. 983-993, 2017.

[50] B. Kim, S. Lee, and J. Kim, "Inverse design of porous materials using artificial neural networks," *Science advances,* vol. 6, no. 1, p. eaax9324, 2020.

[51] S. So, T. Badloe, J. Noh, J. Rho, and J. Bravo-Abad, "Deep learning enabled inverse design in nanophotonics," *Nanophotonics,* vol. 9, no. 5, pp. 1041-1057, 2020.

[52] C. T. Chen and G. X. Gu, "Generative deep neural networks for inverse materials design using backpropagation and active learning," *Advanced Science,* vol. 7, no. 5, p. 1902607, 2020.

[53] A. Paul, P. Acar, W.-k. Liao, A. Choudhary, V. Sundararaghavan, and A. Agrawal, "Microstructure optimization with constrained design objectives using machine learning-

based feedback-aware data-generation," *Computational Materials Science,* vol. 160, pp. 334-351, 2019.

[54] J. Ling, M. Hutchinson, E. Antono, S. Paradiso, and B. Meredig, "High-dimensional materials and process optimization using data-driven experimental design with well-calibrated uncertainty estimates," *Integrating Materials and Manufacturing Innovation,* vol. 6, no. 3, pp. 207-217, 2017.

[55] A. Tran, J. A. Mitchell, L. P. Swiler, and T. Wildey, "An active learning high-throughput microstructure calibration framework for solving inverse structure–process problems in materials informatics," *Acta Materialia,* vol. 194, pp. 80-92, 2020.

[56] A. Peng, X. Xiao, and R. Yue, "Process parameter optimization for fused deposition modeling using response surface methodology combined with fuzzy inference system," *The International Journal of Advanced Manufacturing Technology,* vol. 73, no. 1-4, pp. 87-100, 2014.

[57] M. Raju, M. K. Gupta, N. Bhanot, and V. S. Sharma, "A hybrid PSO–BFO evolutionary algorithm for optimization of fused deposition modelling process parameters," *Journal of Intelligent Manufacturing,* vol. 30, no. 7, pp. 2743-2758, 2019.

[58] S. Deswal, R. Narang, and D. Chhabra, "Modeling and parametric optimization of FDM 3D printing process using hybrid techniques for enhancing dimensional preciseness," *International Journal on Interactive Design and Manufacturing (IJIDeM),* vol. 13, no. 3, pp. 1197-1214, 2019.

[59] S. K. Panda, S. Padhee, S. Anoop Kumar, and S. S. Mahapatra, "Optimization of fused deposition modelling (FDM) process parameters using bacterial foraging technique," *Intelligent information management,* vol. 1, no. 02, p. 89, 2009.

[60] A. K. Sood, R. K. Ohdar, and S. S. Mahapatra, "Experimental investigation and empirical modelling of FDM process for compressive strength improvement," *Journal of Advanced Research,* vol. 3, no. 1, pp. 81-90, 2012.

[61] S. Mahapatra and A. K. Sood, "Bayesian regularization-based Levenberg–Marquardt neural model combined with BFOA for improving surface finish of FDM processed part," *The International Journal of Advanced Manufacturing Technology,* vol. 60, no. 9-12, pp. 1223-1235, 2012.

[62] F. Rayegani and G. C. Onwubolu, "Fused deposition modelling (FDM) process parameter prediction and optimization using group method for data handling (GMDH) and differential evolution (DE)," *The International Journal of Advanced Manufacturing Technology,* vol. 73, no. 1-4, pp. 509-519, 2014.

[63] R. V. Rao and D. P. Rai, "Optimization of fused deposition modeling process using teaching-learning-based optimization algorithm," *Engineering Science and Technology, an International Journal,* vol. 19, no. 1, pp. 587-603, 2016.

[64] O. A. Mohamed, S. H. Masood, and J. L. Bhowmik, "Influence of processing parameters on creep and recovery behavior of FDM manufactured part using definitive screening design and ANN," *Rapid Prototyping Journal,* 2017.

[65] M. S. Saad, A. M. Nor, M. Z. Zakaria, M. E. Baharudin, and W. S. Yusoff, "Modelling and evolutionary computation optimization on FDM process for flexural strength using integrated approach RSM and PSO," *Progress in Additive Manufacturing,* pp. 1-12, 2021.

[66] S. R. Rajpurohit and H. K. Dave, "Prediction and optimization of tensile strength in FDM based 3D printing using ANFIS," in *Optimization of Manufacturing Processes*: Springer, 2020, pp. 111-128.

[67] C. Liu, A. C. C. Law, D. Roberson, and Z. J. Kong, "Image analysis-based closed loop quality control for additive manufacturing with fused filament fabrication," *Journal of Manufacturing Systems,* vol. 51, pp. 75-86, 2019.

[68] C. Liu *et al.*, "Toward online layer-wise surface morphology measurement in additive manufacturing using a deep learning-based approach," *Journal of Intelligent Manufacturing,* pp. 1-17, 2022.

[69] J. Liu, C. Liu, Y. Bai, P. Rao, C. B. Williams, and Z. Kong, "Layer-wise spatial modeling of porosity in additive manufacturing," *IISE Transactions,* vol. 51, no. 2, pp. 109-123, 2019.

[70] P. K. Rao, J. P. Liu, D. Roberson, Z. J. Kong, and C. Williams, "Online real-time quality monitoring in additive manufacturing processes using heterogeneous sensors," *Journal of Manufacturing Science and Engineering,* vol. 137, no. 6, 2015.

[71] C. Liu, Z. Kong, S. Babu, C. Joslin, and J. Ferguson, "An integrated manifold learning approach for high-dimensional data feature extractions and its applications to online

process monitoring of additive manufacturing," *IISE Transactions,* vol. 53, no. 11, pp. 1215-1230, 2021.

[72] D. Amodei, C. Olah, J. Steinhardt, P. Christiano, J. Schulman, and D. Mané, "Concrete problems in AI safety," *arXiv preprint arXiv:1606.06565,* 2016.

[73] T. Moges, G. Ameta, and P. Witherell, "A review of model inaccuracy and parameter uncertainty in laser powder bed fusion models and simulations," *Journal of manufacturing science and engineering,* vol. 141, no. 4, 2019.

[74] F. Lopez, P. Witherell, and B. Lane, "Identifying uncertainty in laser powder bed fusion additive manufacturing models," *Journal of Mechanical Design,* vol. 138, no. 11, 2016.

[75] L. Zhang, G. Yang, B. N. Johnson, and X. Jia, "Three-dimensional (3D) printed scaffold and material selection for bone repair," *Acta biomaterialia,* vol. 84, pp. 16-33, 2019.

[76] C. Mandrycky, Z. Wang, K. Kim, and D.-H. Kim, "3D bioprinting for engineering complex tissues," *Biotechnology advances,* vol. 34, no. 4, pp. 422-434, 2016.

[77] T. J. Hinton *et al.*, "Three-dimensional printing of complex biological structures by freeform reversible embedding of suspended hydrogels," *Science advances,* vol. 1, no. 9, p. e1500758, 2015.

[78] L. Hockaday *et al.*, "Rapid 3D printing of anatomically accurate and mechanically heterogeneous aortic valve hydrogel scaffolds," *Biofabrication,* vol. 4, no. 3, p. 035005, 2012.

[79] S. Gerdes, S. Ramesh, A. Mostafavi, A. Tamayol, I. V. Rivero, and P. Rao, "Extrusion-based 3D (Bio) Printed Tissue Engineering Scaffolds: Process–Structure–Quality Relationships," *ACS Biomaterials Science & Engineering,* 2021.

[80] M. K. Agarwala, V. R. Jamalabad, N. A. Langrana, A. Safari, P. J. Whalen, and S. C. Danforth, "Structural quality of parts processed by fused deposition," *Rapid prototyping journal,* 1996.

[81] S. Gerdes *et al.*, "Process–structure–quality relationships of three-dimensional printed poly (caprolactone)-hydroxyapatite Scaffolds," *Tissue Engineering Part A,* vol. 26, no. 5-6, pp. 279-291, 2020.

[82] A. Conev, E. E. Litsa, M. R. Perez, M. Diba, A. G. Mikos, and L. E. Kavraki, "Machine Learning-Guided Three-Dimensional Printing of Tissue Engineering Scaffolds," *Tissue Engineering Part A,* vol. 26, no. 23-24, pp. 1359-1368, 2020.

[83] N. Martin and G. Youssef, "Dynamic properties of hydrogels and fiber-reinforced hydrogels," *Journal of the mechanical behavior of biomedical materials,* vol. 85, pp. 194-200, 2018.

[84] D. X. Chen, "Extrusion Bioprinting of Scaffolds," in *Extrusion Bioprinting of Scaffolds for Tissue Engineering Applications*: Springer, 2019, pp. 117-145.

[85] L. E. Rustom *et al.*, "Multiscale porosity directs bone regeneration in biphasic calcium phosphate scaffolds," *ACS Biomaterials Science & Engineering,* vol. 3, no. 11, pp. 2768-2778, 2017.

[86] R. Wang, A. Law, D. Garcia, S. Yang, and Z. Kong, "Development of Structured Light 3D-Scanner with High Spatial Resolution and its Applications for Additive Manufacturing Quality Assurance," 2021.

[87] E. Kushan and E. Senses, "Thermoresponsive and Injectable Composite Hydrogels of Cellulose Nanocrystals and Pluronic F127," *ACS Applied Bio Materials,* vol. 4, no. 4, pp. 3507-3517, 2021.

[88] E. Nyberg, A. O'Sullivan, and W. Grayson, "scafSLICR: A MATLAB-based slicing algorithm to enable 3D-printing of tissue engineering scaffolds with heterogeneous porous microarchitecture," *PloS one,* vol. 14, no. 11, p. e0225007, 2019.

[89] D. Girardeau-Montaut, "CloudCompare," *Retrieved from CloudCompare: https://www. danielgm. net/cc,* 2016.

[90] M. Moretti, A. Rossi, and N. Senin, "In-process monitoring of part geometry in fused filament fabrication using computer vision and digital twins," *Additive Manufacturing,* vol. 37, p. 101609, 2021.

[91] T. M. Strat, "Recovering the camera parameters from a transformation matrix," in *Readings in Computer Vision*: Elsevier, 1987, pp. 93-100.

[92] J. Fernandez, A. Singhania, J. Caceres, K. Slatton, M. Starek, and R. Kumar, "An overview of lidar point cloud processing software," *GEM Center Report No. Rep_2007-12-001, University of Florida,* p. 27, 2007.

[93] R. B. Rusu, Z. C. Marton, N. Blodow, M. Dolha, and M. Beetz, "Towards 3D point cloud based object maps for household environments," *Robotics and Autonomous Systems,* vol. 56, no. 11, pp. 927-941, 2008.

[94] P. Cignoni, C. Rocchini, and R. Scopigno, "Metro: measuring error on simplified surfaces," in *Computer graphics forum*, 1998, vol. 17, no. 2: Wiley Online Library, pp. 167-174.

[95] R. B. Rusu, "Willow Garage,«3D is here: Point Cloud Library (PCL),» de Robotics and Automation (ICRA)," in *2011 IEEE International Conference on*, 2011.

[96] R. Polak, F. Sedlacek, and K. Raz, "Determination of FDM printer settings with regard to geometrical accuracy," in *Proceedings of the 28th DAAAM International Symposium*, 2017, pp. 0561-0566.

[97] S. Ramesh *et al.*, "Extrusion bioprinting: Recent progress, challenges, and future opportunities," *Bioprinting,* p. e00116, 2020.

[98] C. R. Hicks, "Fundamental concepts in the design of experiments," 1964.

[99] E. R. Girden, *ANOVA: Repeated measures* (no. 84). Sage, 1992.

[100] I. Bružauskaitė, D. Bironaitė, E. Bagdonas, and E. Bernotienė, "Scaffolds and cells for tissue regeneration: different scaffold pore sizes—different cell effects," *Cytotechnology,* vol. 68, no. 3, pp. 355-369, 2016.

[101] Q. L. Loh and C. Choong, "Three-dimensional scaffolds for tissue engineering applications: role of porosity and pore size," 2013.

[102] W. S. Land II, B. Zhang, J. Ziegert, and A. Davies, "In-situ metrology system for laser powder bed fusion additive process," *Procedia Manufacturing,* vol. 1, pp. 393-403, 2015.

[103] A. Dickins, T. Widjanarko, S. Lawes, and R. Leach, "Design of a multi-sensor in-situ inspection system for additive manufacturing," in *ASPE and EUSPEN Summer Topical Meeting on Advancing Precision in Additive Manufacturing*, 2018.

[104] P. Michaleris, "Modeling metal deposition in heat transfer analyses of additive manufacturing processes," *Finite Elements in Analysis and Design,* vol. 86, pp. 51-60, 2014.

[105] A. J. Dunbar, E. R. Denlinger, M. F. Gouge, and P. Michaleris, "Experimental validation of finite element modeling for laser powder bed fusion deformation," *Additive Manufacturing,* vol. 12, pp. 108-120, 2016.

[106] J. Goldak, A. Chakravarti, and M. Bibby, "A new finite element model for welding heat sources," *Metallurgical transactions B,* vol. 15, no. 2, pp. 299-305, 1984.

[107] M. Gouge, P. Michaleris, and T. Palmer, "Fixturing effects in the thermal modeling of laser cladding," *Journal of Manufacturing Science and Engineering,* vol. 139, no. 1, 2017.

[108] F. Hajializadeh and A. Ince, "Integration of artificial neural network with finite element analysis for residual stress prediction of direct metal deposition process," *Materials Today Communications,* vol. 27, p. 102197, 2021.

[109] M. Megahed, H.-W. Mindt, N. N'Dri, H. Duan, and O. Desmaison, "Metal additive-manufacturing process and residual stress modeling," *Integrating Materials and Manufacturing Innovation,* vol. 5, no. 1, pp. 61-93, 2016.

[110] Y. Liu, J. Zhang, and Z. Pang, "Numerical and experimental investigation into the subsequent thermal cycling during selective laser melting of multi-layer 316L stainless steel," *Optics & Laser Technology,* vol. 98, pp. 23-32, 2018.

[111] G. D. Goh, S. L. Sing, and W. Y. Yeong, "A review on machine learning in 3D printing: applications, potential, and challenges," *Artificial Intelligence Review,* vol. 54, no. 1, pp. 63-94, 2021.

[112] M. A. Mahmood, A. I. Visan, C. Ristoscu, and I. N. Mihailescu, "Artificial neural network algorithms for 3D printing," *Materials,* vol. 14, no. 1, p. 163, 2021.

[113] Y. Wang *et al.*, "StressNet-Deep learning to predict stress with fracture propagation in brittle materials," *Npj Materials Degradation,* vol. 5, no. 1, pp. 1-10, 2021.

[114] Z. Zhou, H. Shen, B. Liu, W. Du, J. Jin, and J. Lin, "Residual thermal stress prediction for continuous tool-paths in wire-arc additive manufacturing: a three-level data-driven method," *Virtual and Physical Prototyping,* vol. 17, no. 1, pp. 105-124, 2022.

[115] C. Li, Z. Liu, X. Fang, and Y. Guo, "Residual stress in metal additive manufacturing," *Procedia Cirp,* vol. 71, pp. 348-353, 2018.

[116] T. A. Rodrigues, V. Duarte, J. A. Avila, T. G. Santos, R. Miranda, and J. Oliveira, "Wire and arc additive manufacturing of HSLA steel: Effect of thermal cycles on microstructure and mechanical properties," *Additive Manufacturing,* vol. 27, pp. 440-450, 2019.

[117] V. Manvatkar, A. De, and T. DebRoy, "Heat transfer and material flow during laser assisted multi-layer additive manufacturing," *Journal of Applied Physics,* vol. 116, no. 12, p. 124905, 2014.

[118] L. Parry, I. Ashcroft, and R. D. Wildman, "Understanding the effect of laser scan strategy on residual stress in selective laser melting through thermo-mechanical simulation," *Additive Manufacturing,* vol. 12, pp. 1-15, 2016.

[119] P. Edwards and M. Ramulu, "Fatigue performance evaluation of selective laser melted Ti–6Al–4V," *Materials Science and Engineering: A,* vol. 598, pp. 327-337, 2014.

[120] A. S. Wu, D. W. Brown, M. Kumar, G. F. Gallegos, and W. E. King, "An experimental investigation into additive manufacturing-induced residual stresses in 316L stainless steel," *Metallurgical and Materials Transactions A,* vol. 45, no. 13, pp. 6260-6270, 2014.

[121] R. Ganeriwala *et al.*, "Evaluation of a thermomechanical model for prediction of residual stress during laser powder bed fusion of Ti-6Al-4V," *Additive Manufacturing,* vol. 27, pp. 489-502, 2019.

[122] B. Zheng, Y. Zhou, J. Smugeresky, J. Schoenung, and E. Lavernia, "Thermal behavior and microstructure evolution during laser deposition with laser-engineered net shaping: Part II. Experimental investigation and discussion," *Metallurgical and materials transactions A,* vol. 39, no. 9, pp. 2237-2245, 2008.

[123] S. Gorsse, C. Hutchinson, M. Gouné, and R. Banerjee, "Additive manufacturing of metals: a brief review of the characteristic microstructures and properties of steels, Ti-6Al-4V and high-entropy alloys," *Science and Technology of advanced MaTerialS,* vol. 18, no. 1, pp. 584-610, 2017.

[124] D. Brown, J. Bernardin, J. Carpenter, B. Clausen, D. Spernjak, and J. Thompson, "Neutron diffraction measurements of residual stress in additively manufactured stainless steel," *Materials Science and Engineering: A,* vol. 678, pp. 291-298, 2016.

[125] M. Strantza *et al.*, "Directional and oscillating residual stress on the mesoscale in additively manufactured Ti-6Al-4V," *Acta Materialia,* vol. 168, pp. 299-308, 2019.

[126] N. Hodge, R. Ferencz, and R. Vignes, "Experimental comparison of residual stresses for a thermomechanical model for the simulation of selective laser melting," *Additive Manufacturing,* vol. 12, pp. 159-168, 2016.

[127] M. Gouge and P. Michaleris, *Thermo-mechanical modeling of additive manufacturing*. Butterworth-Heinemann, 2017.

[128] S. Mazumder, *Numerical methods for partial differential equations: finite difference and finite volume methods*. Academic Press, 2015.

[129] K. He, X. Zhang, S. Ren, and J. Sun, "Deep residual learning for image recognition," in *Proceedings of the IEEE conference on computer vision and pattern recognition*, 2016, pp. 770-778.

[130] F. Chollet, "Keras: The python deep learning library," *Astrophysics source code library*, p. ascl: 1806.022, 2018.

[131] S. B. Kotsiantis, D. Kanellopoulos, and P. E. Pintelas, "Data preprocessing for supervised leaning," *International journal of computer science*, vol. 1, no. 2, pp. 111-117, 2006.

[132] D. P. Kingma and J. Ba, "Adam: A method for stochastic optimization," *arXiv preprint arXiv:1412.6980*, 2014.

[133] I. Bello *et al.*, "Revisiting resnets: Improved training and scaling strategies," *Advances in Neural Information Processing Systems*, vol. 34, 2021.

[134] S. Shah, S. Reddy, A. Sardeshmukh, B. Gautham, G. Shroff, and A. Srinivasan, "Application of machine learning techniques for inverse prediction in manufacturing process chains," in *Proceedings of the 3rd World Congress on Integrated Computational Materials Engineering (ICME 2015)*, 2015: Springer, pp. 261-268.

[135] O. A. Mohamed, S. H. Masood, and J. L. Bhowmik, "Optimization of fused deposition modeling process parameters: a review of current research and future prospects," *Advances in Manufacturing*, vol. 3, no. 1, pp. 42-53, 2015.

[136] J. Jiang, Y. Xiong, Z. Zhang, and D. W. Rosen, "Machine learning integrated design for additive manufacturing," *Journal of Intelligent Manufacturing*, pp. 1-14, 2020.

[137] D. R. Jones, M. Schonlau, and W. J. Welch, "Efficient global optimization of expensive black-box functions," *Journal of Global optimization*, vol. 13, no. 4, pp. 455-492, 1998.

[138] B. Lakshminarayanan, A. Pritzel, and C. Blundell, "Simple and scalable predictive uncertainty estimation using deep ensembles," *Advances in neural information processing systems*, vol. 30, 2017.

[139] X. Qi, G. Chen, Y. Li, X. Cheng, and C. Li, "Applying neural-network-based machine learning to additive manufacturing: current applications, challenges, and future perspectives," *Engineering*, vol. 5, no. 4, pp. 721-729, 2019.

[140] X. Shen, J. Yao, Y. Wang, and J. Yang, "Density prediction of selective laser sintering parts based on artificial neural network," in *International Symposium on Neural Networks*, 2004: Springer, pp. 832-840.

[141] F. Caiazzo and A. Caggiano, "Laser direct metal deposition of 2024 Al alloy: trace geometry prediction via machine learning," *Materials*, vol. 11, no. 3, p. 444, 2018.

[142] J. Zhang, P. Wang, and R. X. Gao, "Deep learning-based tensile strength prediction in fused deposition modeling," *Computers in industry*, vol. 107, pp. 11-21, 2019.

[143] N. Carlini and D. Wagner, "Towards evaluating the robustness of neural networks," in *2017 ieee symposium on security and privacy (sp)*, 2017: IEEE, pp. 39-57.

[144] J. M. Bernardo and A. F. Smith, *Bayesian theory*. John Wiley & Sons, 2009.

[145] X. Yue, Y. Wen, J. H. Hunt, and J. Shi, "Active learning for Gaussian process considering uncertainties with application to shape control of composite fuselage," *IEEE Transactions on Automation Science and Engineering*, vol. 18, no. 1, pp. 36-46, 2020.

[146] G. J. van Houtum and M. L. Vlasea, "Active learning via adaptive weighted uncertainty sampling applied to additive manufacturing," *Additive Manufacturing*, vol. 48, p. 102411, 2021.

[147] S. K. Dasari, A. Cheddad, L. Lundberg, and J. Palmquist, "Active Learning to Support In-situ Process Monitoring in Additive Manufacturing," in *2021 20th IEEE International Conference on Machine Learning and Applications (ICMLA)*, 2021: IEEE, pp. 1168-1173.

[148] D. A. Nix and A. S. Weigend, "Estimating the mean and variance of the target probability distribution," in *Proceedings of 1994 ieee international conference on neural networks (ICNN'94)*, 1994, vol. 1: IEEE, pp. 55-60.

[149] T. G. Dietterich, "Ensemble methods in machine learning," in *International workshop on multiple classifier systems*, 2000: Springer, pp. 1-15.

[150] O. Sagi and L. Rokach, "Ensemble learning: A survey," *Wiley Interdisciplinary Reviews: Data Mining and Knowledge Discovery*, vol. 8, no. 4, p. e1249, 2018.

[151] M. Maftouni, A. C. C. Law, B. Shen, Z. J. K. Grado, Y. Zhou, and N. A. Yazdi, "A robust ensemble-deep learning model for covid-19 diagnosis based on an integrated ct scan images database," in *IIE Annual Conference. Proceedings*, 2021: Institute of Industrial and Systems Engineers (IISE), pp. 632-637.

[152] V. R. Joseph and Y. Hung, "Orthogonal-maximin Latin hypercube designs," *Statistica Sinica*, pp. 171-186, 2008.